remote sensing

Article

A Study on Urban-Scale Building, Tree Canopy Footprint Identification and Sky View Factor Analysis with Airborne LiDAR Remote Sensing Data

Seung Man An

National Territorial Environment & Resources Research Division, Korea Research Institute for Human Settlements, Seoul 30147, Republic of Korea; sm_an@krihs.r.kr; Tel.: +82-44-960-0307

Abstract: Urbanization transforms simple two-dimensional natural spaces into complex three-dimensional (3D) artificial spaces through intense land use. Hence, urbanization continuously transforms vertical urban settings and the corresponding sky view area. As such, collecting data on urban settings and their interactions with urban climate is important. In this study, LiDAR remote sensing was applied to obtain finer-resolution footprints of urban-scale buildings and tree canopies (TCs). Additionally, a related sky view factor (SVF) analysis was performed. The study site comprised an area of Incheon Metropolitan City (501.5 km^2). Results show that the proposed method can be applied to update institutional land maps, enhance land use management, and implement optimized and balanced urban settings.

Keywords: LiDAR; building; tree canopy; urban settings; footprint identification; sky view factor; in situ survey; microclimate; digital twin

Citation: An, S.M. A Study on Urban-Scale Building, Tree Canopy Footprint Identification and Sky View Factor Analysis with Airborne LiDAR Remote Sensing Data. *Remote Sens.* **2023**, *15*, 3910. https://doi.org/10.3390/rs15153910

Academic Editors: Mila Koeva, Christine Pohl and Dessislava Petrova-Antonova

Received: 9 June 2023
Revised: 31 July 2023
Accepted: 3 August 2023
Published: 7 August 2023

1. Introduction

During the urbanization process, urban facilities are sporadically and continuously constructed, and trees are planted and grown in and around buildings, roads, and parks [1–3]. Owing to an acceleration in global climate change, the development of climatically adaptable urban settings has become a major planning and management target. Indeed, the distribution of buildings and trees can impact urban ecosystems and citizens' health [4,5]. Hence, various methodologies have been employed to investigate and estimate their effects in urban climate-friendly utilization settings and for reallocation plans [6–10]. Remote sensing using satellite images and numerical model-based simulations attempts to elucidate the relationship between the distribution of buildings and trees and their environmental impacts on an urban scale [9,11].

Manually investigating individual buildings and trees throughout an entire urban area is difficult [12]. Therefore, satellite and aerial images are widely used. However, they are often limited in their ability to survey the vertical properties of buildings and trees. Hence, three-dimensional point cloud (3DPC) data acquired using Light Detection and Ranging (LiDAR) technology from aerial platforms are employed to cover an urban-scale area, offering new technological survey possibilities for wide and complex urban settings [13–15]. Such surveys provide an opportunity to further improve 3D spatial management by transforming manual processes into automated ones. Consequently, complete automation of continuous surveys and professional analyses is expected [16]. Hence, cartographers' interest in LiDAR for mapping land use and cover is growing [17,18]. Vertical features are particularly interesting in urban studies as urbanization transforms simple two-dimensional (2D) natural spaces into complex 3D artificial spaces through intense land use [19].

Accordingly, the need for integrated urban-scale study tools supporting fine-resolution urban-scale data is growing in urban climate studies. Many researchers have proposed solutions to optimize the identification of urban settings, as well as the simulation of their effects. For instance, the parallelized Large-Eddy Simulation model for urban applications (PALM-4U) and many similar models are widely used. Meanwhile, developmental tools, which can digitalize urban features and provide prompt returns, offer viable solutions with fine resolutions [20]. Nevertheless, their urban-scale support services are dependent on computer resources. Hence, graphical user interfaces (GUIs) have garnered increasing research attention. This has led to the proposals of conducting generally applicable and promptly returnable urban climate analyses [6,9], employing the urban scale high-resolution sky view factor (SVF) as an urban settings indicator [21], and performing user-friendly and inspirable explorations [10,22,23]. However, since most cities are vast and complex, detailed and accurate urban environment analysis data are needed to drive appropriate building and tree management. Although urban digital twin technology will likely serve as a common long-term strategy for identifying large urban settings and conducting interaction analysis, more efficient tools, such as LiDAR remote sensing, are needed for urban-scale approaches.

Hence, the primary aim of this study is to develop a strategy for conducting urban-scale high-resolution identification and analysis by using Airborne LiDAR remote sensing data, with a particular focus on land cover footprint identification and SVF analysis.

2. Materials and Methods

This study proposes a methodology for processing LiDAR 3DPC data acquired from extensive and complex urban-scale areas, enabling building and tree canopy (TC) footprint extraction at various grid sampling resolutions using spatial probability (SP) calculations. A methodology was also integrated based on SVF to analyze potential microclimate induced by buildings or TC. Furthermore, to facilitate easy access to and application of the proposed methodology, a GUI-based platform was developed. GUI-driven urban-scale multi-resolution maps were utilized to address land use/land cover-based urban climate management concerns.

Developed building/TC identification and SVF analysis were compared with land use and land cover maps to verify their usability for current urban planning support. Institutional land use and land cover maps for urban planning and management are currently maintained. Moreover, urban-scale building and FC footprint identification and subsequent SVF analysis results can be applied as auxiliary maps for tentative climate condition diagnoses. For instance, a specific urban region that is relatively vulnerable to a potential extreme heat wave event could be spatially discernable from the whole urban area. Subsequently, an in situ site survey can compare field-based SVF values with LiDAR-based SVF values to measure site microclimate conditions. Although portable instrument-based in situ microclimate attribute measurements typically have low accuracy and, thus, provide limited confidence, they can provide an affordable means to support data interpretation and perform limited verification. Figure 1 presents the overall workflow of this study.

2.1. Airborne Laser Survey (ALS) LiDAR-Based 3DPC Classification

As shown in Figure 1, the first step involved ALS LiDAR 3DPC classification. Building or TC 3DPC object classification requires knowledge about laser return attributes, ground morphology, and land surface phenology. With the laser as a light source, the first return indicates the height of all features, while the last return captures objects lower in the permeable surface, such as the TC [24], under the assumption that TC objects are partially previous in comparison with non-spurious building objects. The morphology of ALS LiDAR 3DPCs was also considered for classification into specific land covers, namely, ground, buildings, or TC. A rule-based automatic classification and manual classification were performed with quality assessment and quality control (QA/QC) to enhance the reliability of the 3DPC classification, after which the verified 3DPCs were entered.

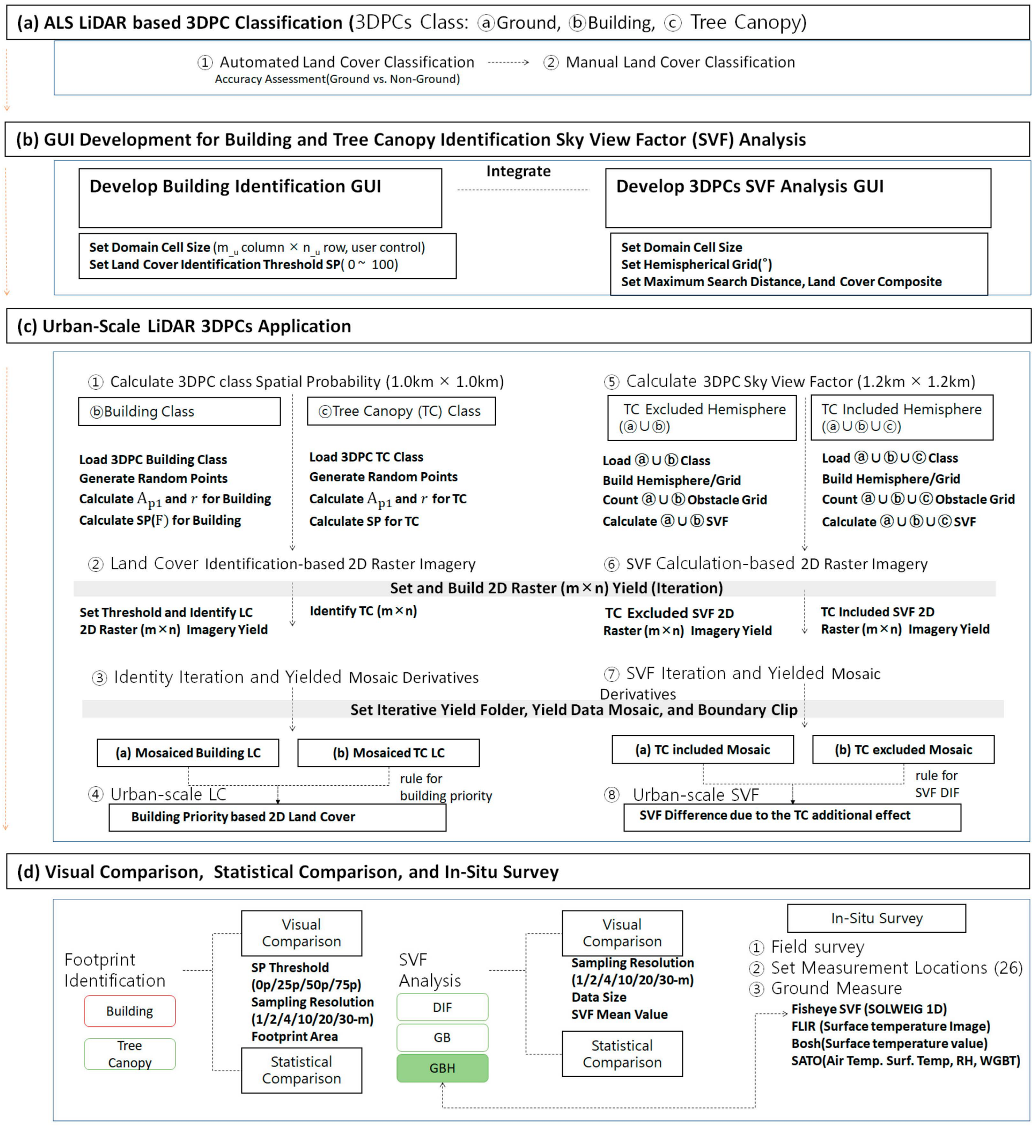

Figure 1. Study workflow. Airborne laser survey (ALS) LiDAR-based 3DPC classification was performed; subsequently, graphical user interface (GUI) development for building/tree canopy (TC) identification and sky view factor (SVF) analysis was performed. LiDAR-based Urban scale maps were generated, and visual/statistical comparisons were made, followed by an in situ survey.

2.2. GUI Development for Footprint Identification and SVF Analysis

The second step (Figure 1b) involved GUI development for footprint identification and SVF analysis. The two methods and algorithms proposed by An et al. [13] and Yi and An [25] were integrated into a single GUI. SP-based building and TC footprint identification require specification interfaces, such as setting user-defined spatial sampling and SP thresholds for identification. SVF analysis also requires an interface, such as setting spatial sampling, SVF analysis configurations, including ground with other land cover class composites, hemispherical grid resolving power, and the maximum search distance of the classified 3DPCs from each cell center (observation location). Qt and Microsoft Foundation Class libraries were used to develop an integrated GUI to meet the required development goal. Qt is a cross-platform application-programming framework for GUI and non-GUI applications. The 3DPC format input and output (I/O) development is referred to as the LAS specification version 1.4-R15 [26].

2.2.1. Land Cover Identification

Yi and An [25] proposed a cell-based SP calculation for building and sequential footprint identification methods from classified LiDAR 3DPCs. The major change applied in the current study regarding conversion to rasterized footprints was the expansion of land cover to buildings and TC. The Monte Carlo Integration (MCI) technique was applied for 3DPC base SP calculations. In this method, random numbers are applied as a technical solution [27] by obtaining a probabilistic approximation from a mathematical equation or model [28]. This was applied to convert land cover class 3DPCs from a user-specified cell into an SP value; that is, a cell is not considered a determined space but rather a space to be determined probabilistically. Hence, MCI-based SP calculations represent a specific land cover area ratio per cell as relative shares per cell area. The SP in each cell area was calculated from the classified building or TC 3DPCs using Equations (1)–(4). Notably, these equations are coded to batch the standardized LiDAR files through GUI (Figure 2a).

$$r = \sqrt{\frac{\mathrm{A_{p1}}}{\pi}} \tag{1}$$

where r is the interactive search distance variable applied according to the spatial density of each 3DPC cell dataset. Meanwhile, r is applied to enumerate randomly generated points in a cell and is dependent on A_{p1} (the length is shorter than the cell sampling size (Figure 2c). Logically, the number of classified 3DPCs is less than the number of randomly generated points. For instance, Figure 2c shows 5 LiDAR points classified as building and 33 randomly generated points in a cell. Moreover, r should consider Airborne LiDAR irregular 3DPC distribution and heterogeneous real land cover; there were few LiDAR points in the water area. Hence, A_{p1} is introduced to exclude empty cells and calculate r reflecting the empty cell distribution in the whole array. That is, A_{p1} (unit: m^2) represents the effective cell area excluding empty cells (the average cell area over the available cells) and is calculated as follows:

$$A_{p1} = \frac{(\mathrm{cell_x} \times \mathrm{cell_y}\ ) - \mathrm{m_{cell}}}{\mathrm{n_p}}, \tag{2}$$

where $cell_x$ and $cell_y$ are the array numbers of cells along the horizontal and vertical boundaries, respectively; m_{cell} is the number of empty cells (e.g., water area cells in Figure 2); and n_p is the total number of 3DPCs generated in the cell. SP represents the spatial probability of the cell and is calculated as follows:

$$SP = \int \mathrm{f(x)d_x} \cong \frac{1}{\mathrm{N}} \sum\nolimits_{i=1}^{n} \rho(\mathrm{x_i}, \mathrm{y_i}), \tag{3}$$

where f(x) is a function composed of the interactive search distances and the coordinates ($\mathrm{x_{LIDAR}}$, $\mathrm{y_{LIDAR}}$) of each LIDAR point; $\mathrm{x_{LIDAR}}$ is the x-coordinate of the LiDAR point, and $\mathrm{y_{LIDAR}}$ is the y-coordinate of the LiDAR point; N is the number of random points generated in cell (x_i, y_i); x_i is the x-coordinate of random point i; and y_i is the y-coordinate of random point i. A computationally economical and efficient number of random points (33 random points per cell area) was used to calculate SP. The more random points are generated, the more reliable SP is, and the longer the calculation time to obtain results. The function $\rho(\mathrm{x_i}, \mathrm{y_i})$ detects the presence or absence of a specific land cover 3DPC at the 33 randomly generated points (Figure 2c) and is obtained using the following formula:

$$\rho(\mathrm{x_i}, \mathrm{y_i}) = \begin{cases} 1 & \sqrt{(\mathrm{x_{LIDAR}} - \mathrm{x_i})^2 + (\mathrm{y_{LIDAR}} - \mathrm{y_i})^2} \leq \mathrm{r} \\ 0 & \text{otherwise} \end{cases}, \tag{4}$$

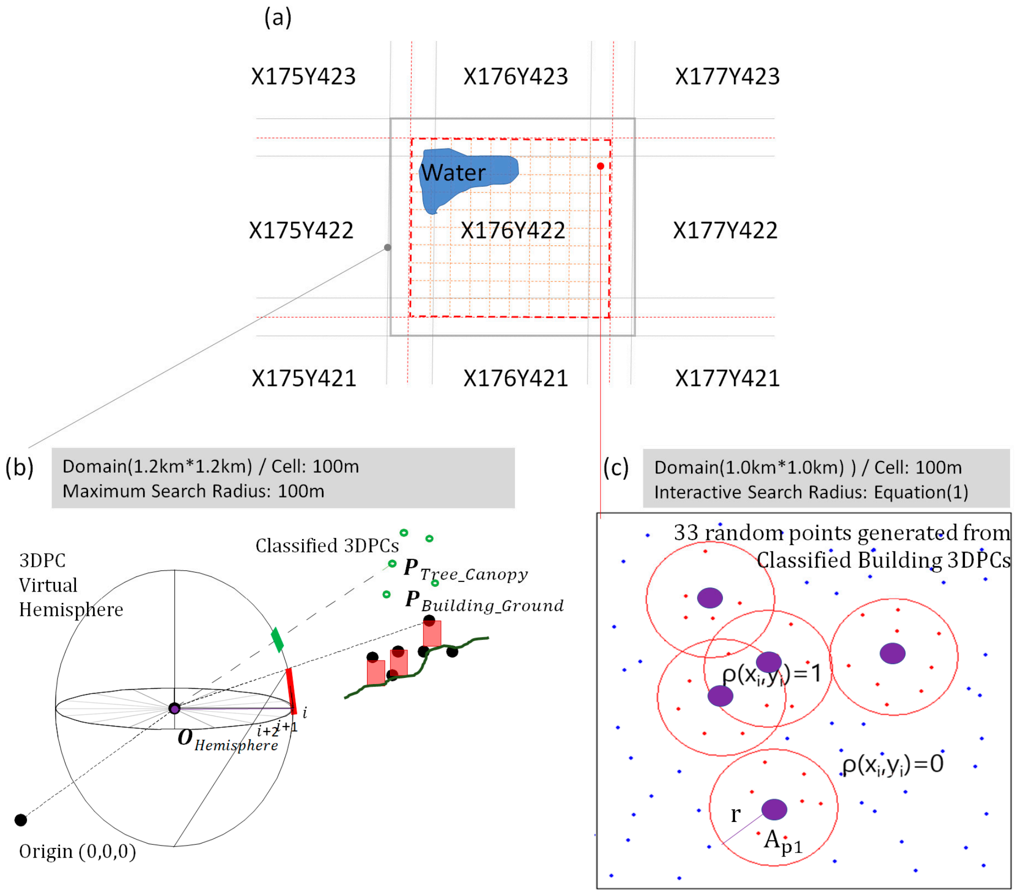

Figure 2. Concept of LiDAR 3DPC-based graphical user interface (GUI) allocation for land cover identification and sky view factor (SVF) analysis. (**a**) Square domain indexing and grid-based cell array setting. (**b**) Cell-based SVF calculation; red line covers the ground or building, and the green line covers the tree canopy (Source: An et al. [13]); empty cells like water area are excluded when A_{p1} is calculated. (**c**) Cell-based SP calculation; rectangle represents a cell, identified points appear in the red circles (generated from purple LiDAR points and search distance) and the other blue points outside circles (Source: Yi and An [25]).

2.2.2. SVF Analysis

The SVF measures the shielding amount of all objects visible in the sky view above a certain location to estimate the sky (diffuse) radiation reaching that location from a virtual sky hemisphere. Hence, it is a dimension-reduced urban canopy parameter that captures 3D forms through horizon limitation fractions [29]. An et al. [13] reviewed the SVF calculation method and proposed a 3DPC-based SVF calculation for specialized TC analysis, expecting that all related processes will soon be automated (Equation (5)).

$$\mathrm{SVF}_{3DPC} = 1 - \text{Obstacle Grid Ratio}, \tag{5}$$

The LiDAR 3DPC object detects virtual obstacles that are oblique, such as a building, and partly transparent, such as a TC [30]. In accordance with the classified LiDAR 3DPCs, An et al. [13] proposed a virtual hemisphere for the projected sustaining disk, particularly for 3DPC-based SVF calculations. The 2D sustaining disk consists of polar matrices (array of cells), and each cell count classifies 3DPCs as a shielding obstacle from the hemisphere's origin (observing point); Equation (6) shows Obstacle Grid Ratio (0–1).

$$\text{Obstacle Grid Ratio} = \frac{\sum i \sum j \cdot \rho(i,j) \cdot S(i,j)}{\sum i \sum j \cdot S(i,j)}, \tag{6}$$

where $\sum i \sum j \cdot S(i,j)$ is the total area of the sustaining disk and $S(i,j)$ is the projected area of each hemispherical grid cell. The sustaining disk had three layers to separately calculate the three classified 3DPCs (ground, building, and TC). When three classified 3DPCs were detected in each cell on a sustaining disk, the cell was considered opaque (Figure 2b).

$$\rho(i,j)_{(ground, Building, Tree\ Canopy)} = \begin{cases} 1 & N(i,j) > 0 \\ 0 & \text{otherwise}' \end{cases} \tag{7}$$

where ρ is the conditional function that determines whether the classified 3DPC is in the grid; $N(i,j)$ is the number of points that lie on cells (i,j); i is the index of the longitudinal unit angle; and j is the index of the latitude unit angle. In addition, when the conditional cell value relating to ground or building class 3DPC was calculated as the oblique $(\rho = 0)$, all other vertical cells below the oblique cell were identified as the oblique (Figure 2b). Equations (5)–(7) are coded to batch the standardized LiDAR files through GUI (Figure 2a).

2.3. Application of Urban-Scale LiDAR 3DPCs

2.3.1. Study Area

The area for the urban-scale LiDAR 3DPC application study was Incheon Metropolitan City. Incheon is located in the northwestern region of South Korea, bordering the Seoul and Gyeonggi provinces (Figure 3a,b). The study area covers the primary regions of Incheon Metropolitan City, encompassing 501.5 km^2, excluding Ganghwa and Ongjin. This includes four administrative districts, including inland areas and islands, such as Yeongjong Island (Figure 3c). Incheon was a rapidly growing urbanized city. However, the population is slowly decreasing [31]. In 1883, the population of Incheon was approximately 5000, whereas the current urban area is home to approximately three million residents, making it the third most populous city in South Korea, after Seoul and Busan. Intensive urban-scale land use was employed to capitalize on its natural advantages of being a coastal city and its proximity to the capital area for growth. Incheon operates the Incheon International Airport and Incheon Port, positioning itself as a crucial transportation hub in Northeast Asia. Furthermore, since 2003, Incheon has been promoting extensive urban land development as a large-scale smart free economic zone, the Incheon Free Economic Zone [32]. The urban settings and sky view area of Inchon continue to change.

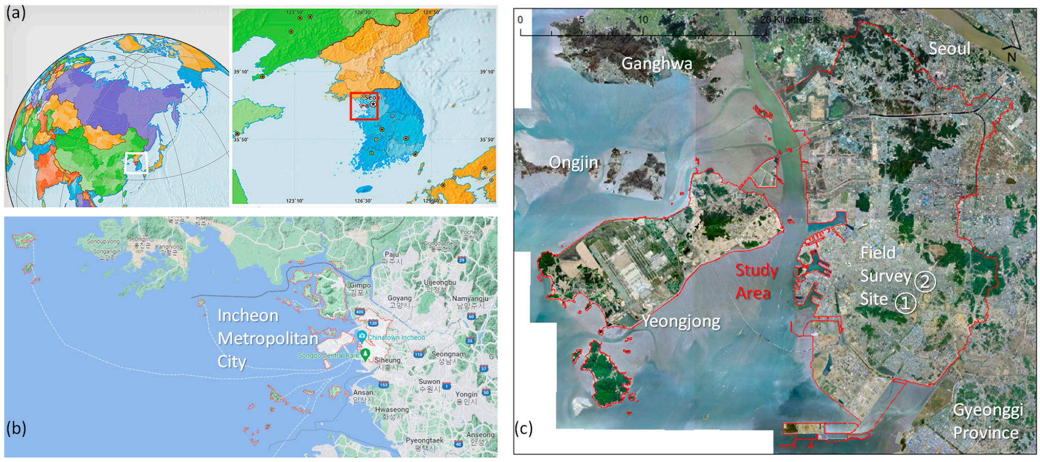

Figure 3. Study area, Incheon, South Korea. (**a**) The geographical location of the Incheon Metropolitan City "http://www.maphill.com/korea-south/inchon/location-maps/political-map/ (accessed on 8 June 2023)"; (**b**) Administrative area, including inland, two large islands, and other islands "https://www.google.com/maps/place/Incheon (accessed on 8 June 2023)"; (**c**) Area where LiDAR 3DPCs were employed; ① and ② are in situ site survey sites.

2.3.2. Data Collection

Table 1 lists the datasets used in the study. As the key input of this study, the LiDAR 3DPCs were acquired from the ALS project, which is a part of the National Geographic Information Institute (NGII) survey program. From 2002 to 2021, NGII performed ALS surveys to build LiDAR 3DPCs that cover the entire urban area of Korea. Informal rules are driven by iterative testing and refinement for the automated building or TC classification. Subsequently, a quality control method developed by NGII was applied. Other GIS datasets, such as land use (zone) and land cover, were also used for overlay-based statistical comparisons or visual comparisons as an auxiliary reference.

Table 1. The data input applied in this study.

Data	Provider	Use Purposed
Airborne LiDAR Map (3DPC)	NGII	Buildings and tree canopy (TC) footprint identification and SVF analysis
Administrative Area	MOLIT	Study Area Extraction
3DPC Index Map	User-defined	LiDAR 3DPCs Data Partitioning and Integration (Mosaic)
Digital Ortho Photo Map	NGII	Superficial comparison and visual interpretation
Land Cover	ME	TC footprint reference, overlay analysis
Land Use (Zone)	MOLIT	Land use overlay analysis
Building	NGII	Building footprint reference, overlay analysis

ME: Ministry of Environment (https://egis.me.go.kr, accessed on 8 June 2023); MOLIT: Ministry of Land, Infrastructure, and Transport; NGII: National Geographic Information Institute (https://map.ngii.go.kr, accessed on 8 June 2023).

Processing the LiDAR data of the study area proved challenging as the 3DPC dataset covers an area of over 500 km^2, making it difficult to manipulate as a workbench input. Hence, distributed processing with a parallel calculator that supports a GUI was required for efficient manipulation. A 3DPC Index Map was constructed manually to segment the massive 3DPC data provided by NGII (approximately 2.7 km $\times$ 2.7 km, 1:5000 scale) into smaller data (1.2 km $\times$ 1.2 km) and re-allocate the non-rectangular domain to a square domain (Figure 2a). TerraScan and TerraModel V.009.001, MicroStation V8-based third-party commercial software, were used. Consequently, 750 3DPC files with equal domain areas were generated using the 3DPC Index Map. Digital ortho photo maps provided by NGII were available for Incheon as a supporting dataset and were incorporated into the classification. These did not contain a near-infrared band, and only visible RGB bands were available. High-resolution ortho-imagery (0.25 m) acquired in 2012, 2014, and 2016 were used for visual interpretation. Additionally, thematic land cover maps provided by the Ministry of Environment (ME) and Land Use (zone) maps (Table 2) provided by the Ministry of Land, Infrastructure, and Transport (MOLIT) were used to derive an overlay analysis based on zonal statistical comparisons.

2.3.3. Urban-Scale LiDAR 3DPCs Processing

The development of an integrated GUI is not only for integration but also for expansion, enhancing the function with an upgraded menu from the previous GUI [13,25]. After validating the developed GUI, all 750 3DPC files were input as bundles into the GUI for iterative batch processing to calculate the 3DPC class SP. As shown in Figure 1c, 750 classified 3DPC files were sequentially processed for footprint identification and SVF analysis. All classified 3DPCs were allocated to each cell in the sampling grid by referencing the coordinates and applying the equations. Following the GUI specification, all data I/Os were processed using the visualized GUI.

Table 2. Land use (zone) map data properties and coverage area in the study site.

Class 1	Class 2	Class 3	Code	Land Use Purpose	Area (km^2)
Urban areas	Residential	Class I exclusive	UQA111	Protect residential environments for independent housing	1.18
		Class II exclusive	UQA112	Protect residential environments for multi-unit housing	1.77
		Class I general	UQA121	Create convenient residential environments for low-floor housing	14.6
		Class II general	UQA122	Create convenient residential environments for mid-floor housing	47.55
		Class III general	UQA123	Create convenient residential environments for mid/high housing	46.21
		Quasi-residential	UQA130	Provide commercial environments to residential areas	21.44
	Commercial	Central	UQA210	Expand the commercial functions in the center/sub-center	3.6
		General	UQA220	Provide general commercial and business functions	22.41
		Neighboring	UQA230	Supply the daily necessities and services in the neighboring area	0.43
		Circulative	UQA240	Increase the circulation function in the city and between the areas	1.04
	Industrial	Exclusive	UQA310	Admit the heavy chemical industry, pollutive industries, etc.	0.07
		General	UQA320	Allocate industries not impeditive to the environment	36.04
		Quasi-industrial	UQA330	Admit light industry and other industries, but in need of supplementing the residential and commercial functions	25.83
	Green	Conservation	UQA410	Protect natural environment and green areas in the city	45.18
		Agricultural	UQA420	Reserve an area for agricultural production	3.9
		Natural	UQA430	Secure green area space and supply of future city sites	232.73
Management areas	Conservation and management		UQB300	Protect, but hard to designate as conservation areas	1.01
	Agricultural and management		UQB200	Reserves for agriculture and forestry	0.17
	Development and management		UQB100	Incorporate to future urban areas	12.37
Agricultural areas			UQC001	Protect forestry and promote agriculture	5.93
Natural environment conservation areas			UQD001	Protect natural environment	0

Source: OECD [33].

The first step was identification processing. The building and TC footprints were identified when the calculated SP value was higher than the threshold value specified by the user in the GUI. Using the GUI, various resolving powers of the cell size (1, 4, 10, and 30 m) and SP-based identification threshold limits (over 0, 25, 50, and 75) were applied. Consequently, GUI-specified identification footprint datasets were obtained. Iteratively yielded 2D raster footprint identification datasets (ASCII format) were accumulated to the specific directory of the mosaic, and the yielded results were compared according to the resolving power of the cell (1–30 m) and the SP threshold (0–100). The building and TC footprint identification datasets were mosaiced onto an urban-scale 2D raster. However, footprint cells can be identified not only as buildings but also as TC. In this case, as a rule, even though the building SP was smaller than the TC SP, the building class was prioritized to avoid losing building identification due to the few and sparsely distributed building footprints. The rule is typically applied to map generalization for buildings as identification of buildings is important for conventional map use. However, although it is computationally applicable for a monotonous land cover cell, problems can arise in a heterogeneous land cover cell owing to the one-sided decision. In footprint identification computation, each cell is allocated from the user-specified spatial sampling resolutions (1, 2, 4, 10, 20, and 30 m) as a grid array and measured. To compare the identified building and TC footprint areas derived from different spatial sampling resolutions and minimum thresholds (P0, P25, P50, and P75), the identified values were registered in the specified grid aster files. Directory-based batch processing enabled the sequential iterative yield of the identified building and TC footprint raster files from the classified 3DPC files created in the optional cases named directory.

The second step was SVF analysis processing, which quantifies the effect of a spatially distributed urban-scale TC on the SVF as a climate indicator. Hence, two sets of classified 3DPCs were prepared as composites by the GUI specification: one set included the ground and buildings, and the other included the ground, buildings, and TC. The center of each cell is the location of the input land cover observation, and the user-defined maximum search distance determines the radius of the virtual hemisphere. An et al. [13] suggested that a maximum search distance-based buffer masking area longer than 60 m was required to remove errors and yield numerous pixels of SVF analysis grid data. Ideally, the SVF analysis should include all geometrically visible 3DPCs to consider all obstacles as far away as possible. In this study, the SVF analysis domain coverage was 1.2 km × 1.2 km (Figure 2a,b). Hence, a maximum search distance of 100 m was applied, considering various urban topographies and vertical urban environments. Two sets of classified 3DPC composites were projected onto a 3D hemisphere and re-projected onto a 2D sustaining disk for area-based calculations. Computationally, two types of the SVF value were derived using Equations (5)–(7), and each cell composing a user-specified grid array was measured. To compare the presence (GBH) or absence (GB) of the TC per 3DPC file, these values were registered into two raster format (ASCII) files. In addition, directory-based batch processing enabled the sequential iterative yield of SVF raster files from differently specified 3DPC files. From the GUI, the specified resolving power of the cell size (1, 4, 10, and 30 m) was applied to the classified 3DPCS bundle files, and several sets of SVF analysis 2D raster data were obtained iteratively and accumulated into the specified directory.

2.4. Visual and Statistical Comparison

The visual and statistical comparison experiments have two purposes: to describe the specified GUI application results and determine the applicability and challenges of the urban-scale fine-resolution methodology employed with massive LiDAR 3DPC data. Hence, each of the 750 raster grid files was mosaiced onto urban-scale map images for visual and statistical comparison. Each mosaic was created using a Python script-based ESRI ArcGIS geospatial function (raster mosaic) batch. The identified footprint mosaic iteratively yielded six different sampling resolutions and four minimum thresholds based on raster imagery files that were mosaiced into the urban-scale high-resolution building and TC footprint maps. The SVF mosaic iteratively yielded four = sampling resolutions (1, 4, 10, and 20 m) and three analysis types (TC presence, TC absence, and SVF difference). The raster imagery files were mosaiced into urban-scale high-resolution SVF maps. Two types of urban-scale SVF analysis imagery (TC vs. TC excluded) were applied as inputs to the subtraction function to measure the SVF difference and quantify the TC effect. This showed an additional decrease in the SVF value owing to the presence of the TC in the urban environment as a quantitative view of the sky.

The mosaiced urban-scale building and TC footprint maps made from different resolutions and SP thresholds, and the urban-scale SVF made from different resolutions and vertical feature composites, were visually compared. In addition, Incheon Central Park zoom-in visual verification and in situ field surveys were performed. Statistical comparisons using urban-scale mosaic map data overlay analysis with GIS maps (building footprint digital map, land cover, and land use) were performed to derive quantitative values of the identified vertical feature footprint areas and related TC SVF effects.

2.5. In Situ Survey

An in situ survey was performed to compare the 3DPC SVF values (GBH, 1 m resolution) with others. The optical SVF measurements method was employed to conduct a field survey for 26 locations during the hot and sunny period of July 2023 (Figure 4). Sky view fish-eye images were captured at sunset (17:00–20:00) on 6 July 2023 with a Canon EOS 6D MarkII camera with SIGMA 8 mm F3.5 circular fish-eye lens. Before taking fish-eye images, the camera was mounted on a Manfrotto tripod, horizontally aligned, and oriented true north using a portable level and electronic compass. Twenty-six fish-eye images (Figure 4a) were converted from color to black and white by altering the brightness and contrast of each image using the threshold control interface in SOLWEIG 1D v.1.0. Fish-eye image-driven SVF indicates the degree of open sky area from an observation focal point 0.9 m above ground level. The SVF is influenced by surrounding buildings, tree canopy cover, and other street furniture objects. Additionally, microclimate measurements were performed at 11:30–13:30 on 7 July 2023 with three portable surveying instruments (Table 3). A hollowed black sphere with a temperature sensor inside a portable instrument (SATO SK-170GT) measures air temperature (TA), relative humidity (RH), wet bulb globe temperature (WBGT), and globe temperature (TG). The black globe was equilibrated to the measurement location conditions for 3 min. FLIR TG267 was then used to capture surface temperature images from the radiance of surrounding urban settings or landscapes. BOSCH GIS 500 and FLIR TG 267 were used to measure ground surface temperatures. Additionally, we recorded certain attribute values for the ground surface material type (wood, granite, loam, asphalt, cement concrete), shadow condition at the time of measurement (shadowy, sunlit), canopy type (open, tree, parasol), and land use zone codes.

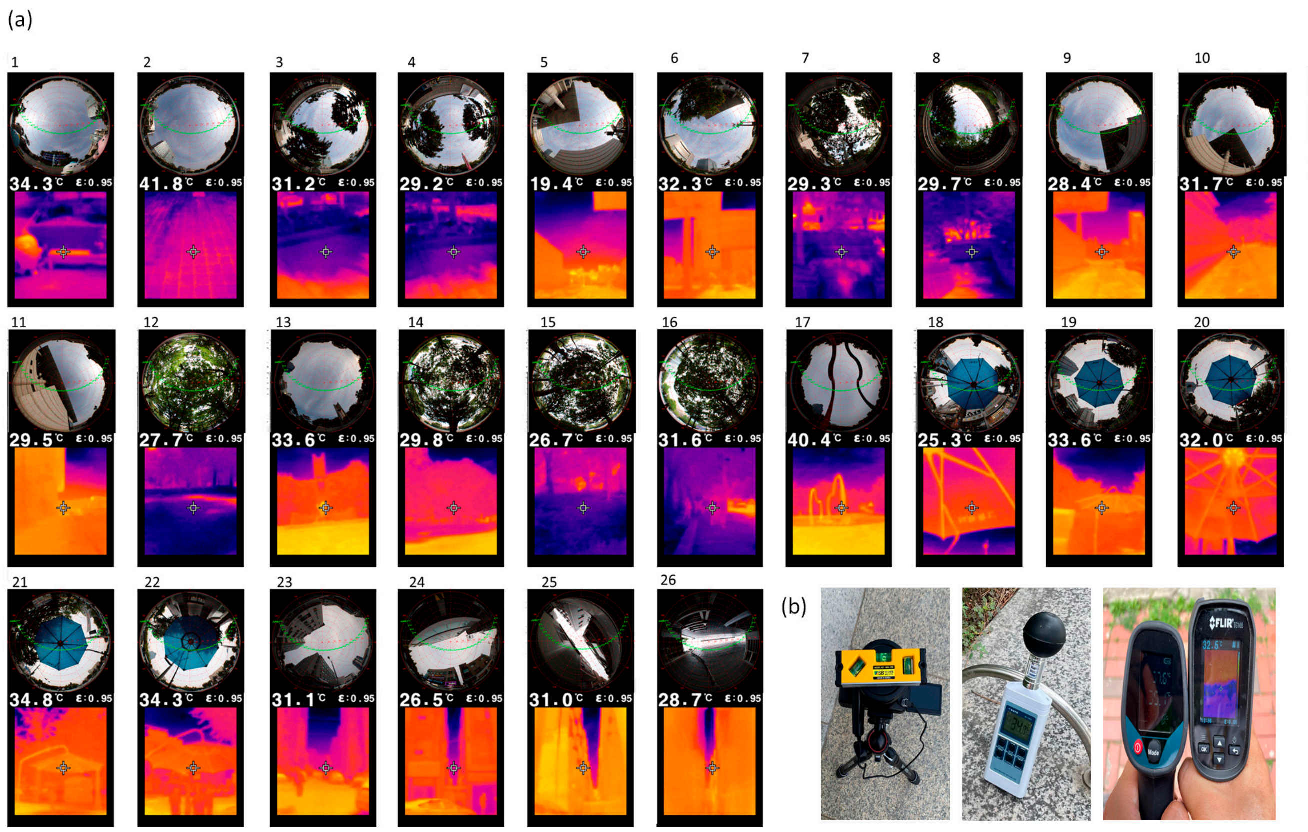

Figure 4. Fish-eye photography and surface temperature images were collected from 26 sites. (**a**) 26 Fish-eye sky view images (camera focal center heights above the ground 0.9 m) and surrounding landscape surface temperature mages (FLIR TG267); (**b**) Set-up for fish-eye photography acquisition and relevant surface temperature measurement (SATO SK-170GT, BOSCH GIS 500 and FLIR TG267).

Table 3. Specification for the portable microclimate measurement instruments used in this study.

Climate Attributes	Measurement Instrument	Measurement Range (Accuracy)
Air Temperature (TA)	SATO SK-170GT	0–50 °C (±0.6 °C)
Relative Humidity (RH)	SATO SK-170GT	10–95% (±3.0%)
Wet Bulb Globe Temp. (WBGT)	SATO SK-170GT	0–50 °C (±2.0 °C)
Globe Temperature (TG)	SATO SK-170GT	20–60 °C (±1.2 °C)
Surface Temperature	BOSCH GIS 500	−30–500 °C (±1.8 °C)
Surface Temperature Image	FLIR TG 267	−25–380 °C (±3.0 °C)

3. Results

3.1. LiDAR 3DPCs Graphical User Interface

For the analysis of advanced urban-scale settings, the GUI developed LiDAR 3DPC data for interactive virtual exploration and provided user-specified batch data via the generation of simple windows (Figure 5a,b). In GUI, LiDAR data I/O were logged on an independent console window (Figure 5c). Figure 5d shows snapshots of the uploading and navigation screens of one LiDAR file (1.2 km × 1.2 km). Users can assign a hemispherical origin on the ground, project 3DPCs onto a virtual hemisphere, and visualize during the virtual 3DPCs space exploration. Although GUI facilitates the acquisition of information for knowledge development, service functions are insufficient. As described by An et al. [13], the rule for assigning 3DPCs (allocation) is not flexible; this results in the terrain being assigned first, followed by the buildings and finally, the TC.

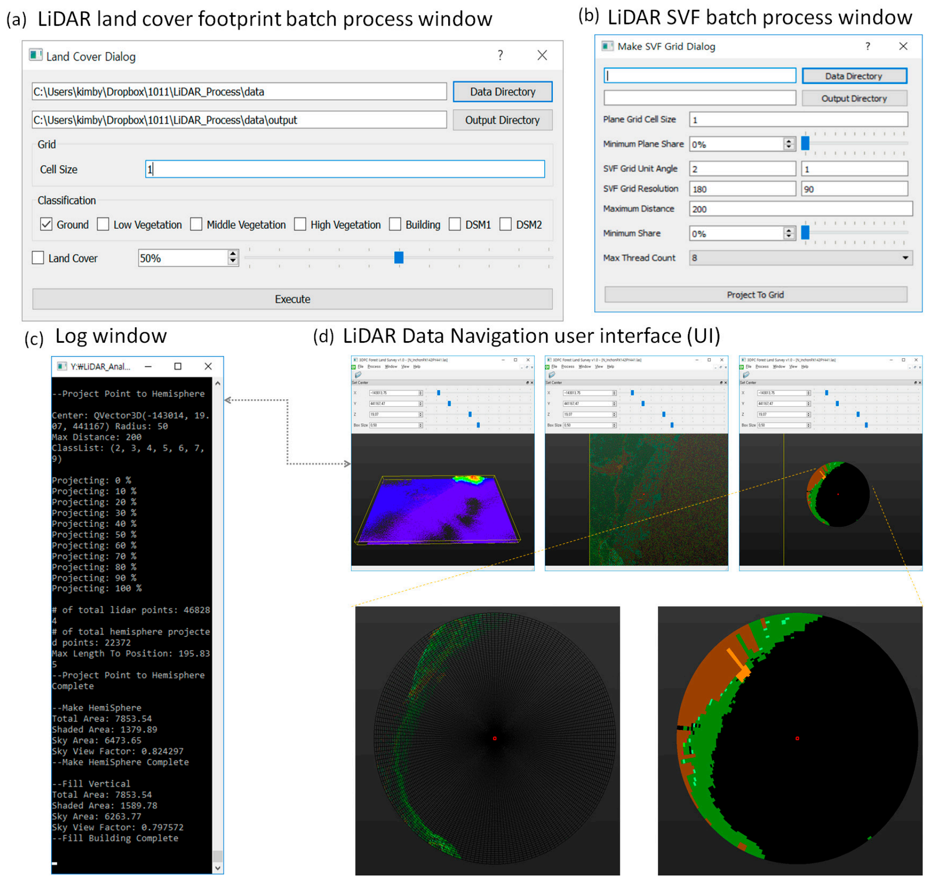

Figure 5. Development of LiDAR 3DPC input and output (I/O) GUI. (**a**) I/O directory, sampling resolution (cell size), land cover class, threshold (%), etc., for footprint identification. (**b**) User I/O directory, sampling resolution (cell size), land cover class, threshold (%), etc., for SVF analysis. (**c**) Console window view of the log according to user control. (**d**) Single LiDAR dataset can be visualized on GUI to explore virtual 3DPC space. In addition, a virtual sky view projected on the sustaining disk through the hemispher at the observation point is used as an auxiliary data.

3.2. Urban-Scale Building and Tree Canopy Footprint

Urban-scale building and TC footprint identification results were successful as the GUI-based workbench promptly produced urban-scale map data for a targeted resolution. In total, 750 classified 3DPC files in the directory were affordable inputs for urban-scale LiDAR 3DPC applications. Each SP was calculated from a GUI-specified resolution, and the identified footprint was produced over several hours to a few days. As shown in Figure 6, 36 mosaiced urban-scale buildings and TC footprint maps, arrayed as a series of image spreadsheets, were expressed with different visual information for the study area. The superficial comparison results revealed that urban-scale outputs showed a gradual decrease in identifiable footprints, demonstrating visually lowered clarity or blurred images as the GUI specifies a higher SP threshold or finer resolution. Hence, finding optimized GUI composite options to obtain the best area (km^2) fitted building or TC footprint is challenging. Typically, a true or reference value is required for the overall accuracy assessment of the identified footprint area. Unfortunately, the true land cover footprint area of buildings or TC is unclear due to difficulty in measuring the in situ footprint. This is primarily due to the non-geometric forms of urban vertical features and complex urban settings. Hence, a uniform threshold application should be avoided. Each file-based or LiDAR land cover class-based threshold application can be recommended.

According to the building class national digital map of Korea (NCA_B0010000, 1/5000 scale) provided by the NGII, the total building footprint of the study area covers approximately 48.68 km^2, which excludes many temporary buildings. Only overlaying and comparing the manually digitalized building footprint (NCA_B0010000) with the LiDAR 3DPC GUI-generated building footprint may be inappropriate as they have different mapping rules and steps. NCA_B0010000 has unique and complicated classification codes and was manually edited using in situ field survey auxiliary data. Building or TC 3DPCs were also manually classified; however, the classification was simple and skipped in situ field surveys. In addition, most 3DPCs below 2 m above the ground were not used, exacerbating the difference. Although these differences are significant, we roughly set the true value zone of the building footprint for the study area as 40–100 km^2. Additionally, this study assumed that the true value of the TC footprint area was 80–160 km^2, which was referred from the forest class land cover area (89.23 km^2) provided by the Ministry of Environment (Table 4).

Table 4. Land cover map data properties by classification level and coverage area in the study site.

Level 1			Level 2			Level 3		
Name	**Code**	**Area (km^2)**	**Name**	**Code**	**Area (km^2)**	**Name**	**Code**	**Area (km^2)**
Built-Up Land	100	175.70	Residential	110	20.68	Single-Family Units	111	10.10
						Multi-Family Units	112	10.58
			Industrial	120	15.23	Industrial	121	15.23
			Commercial	130	15.96	Commercial	131	15.92
						Complexes	132	0.04
			Communication	140	2.08	Communication	141	2.08
			Transportation	150	113.12	Airport	151	0.70
						Harbor	152	3.73
						Railroad	153	1.10
						Road	154	107.54
						Other	155	0.05
			Public Utilities	160	8.64	Environmental	161	0.50
						Educational	162	2.42
						Other	163	5.72
Agricultural Land	200	44.50	Paddy Field	210	18.07	Readjustment	211	8.64
						Non-Readjustment	212	9.43
			Non-Irrigated Land	220	20.98	Readjustment	221	1.42
						Non-Readjustment	222	19.56
			Protected Cultivation	230	2.83	Protected Cultivation	231	2.83
			Orchard	240	1.15	Orchard	241	1.15
			Other Cropland	250	1.47	Ranch or Farm	251	0.20
						Other	252	1.27
Forested Land	300	82.93	Deciduous Forest Land	310	51.95	Deciduous Forest Land	311	51.95
			Coniferous Forest Land	320	19.01	Coniferous Forest Land	321	19.01
			Mixed Forest Land	330	11.98	Mixed Forest Land	331	11.98

Table 4. *Cont.*

Level 1			Level 2			Level 3		
Name	**Code**	**Area (km^2)**	**Name**	**Code**	**Area (km^2)**	**Name**	**Code**	**Area (km^2)**
Grassland	400	73.93	Natural Grassland	410	0.86	Natural Grassland	411	0.86
			Non-Natural Grassland	420	73.07	Golf Course	421	4.25
						Cemetery	422	2.86
						Other	423	65.96
Wetland	500	23.56	Inland Wetland (Wetland Vegetation)	510	15.11	Inland Wetland (Wetland Vegetation)	511	15.11
			Coastal Wetland	520	8.46	Tidal Flat	521	7.68
						Salt Field	522	0.77
Barren Land	600	82.98	Natural Barren Land	610	1.88	Beach	611	1.23
						Riverside	612	0.26
						Exposed Rock	613	0.39
			Non-Natural Barren Land	620	81.09	Quarry	621	0.20
						Playground	622	2.34
						Other	623	78.56
Water	700	19.50	Inland Water	710	13.76	Stream and Canal	711	5.33
						Lake and Reservoir	712	8.44
			Seawater	720	5.74	Seawater	721	5.74

Source: NGII [34].

Despite the true value zone wide range set, many identified footprint area values have exceeded the range significantly (Figure 7 and Table 5). As shown in Figure 7a, the chart of the 36 urban-scale building footprint area (km^2) values derived from the GUI and applied to the classified LiDAR 3DPCS demonstrates the difficulty in identifying building footprints. Limited parts of the urban-scale building footprint area (km^2) P0 and P25 values were in the true value zone, whereas none of the P50 and P75 values reached the true value zone. In the P0 case, the 2 m- and 4 m-based area values were within the true value zone. Both underestimation (1 m) and overestimation with steep linear trends were evident, indicating that the P0 building footprint area values were sensitive to resolution variation. However, in the P25 case, the 10 m-, 20 m-, and 30 m-based values were in the true value zone. Both underestimations (1, 2, and 4 m) were evident. However, the P25 building footprint area values were less sensitive as the resolution became coarser. Hence, we can conclude that when using the given classified building 3DPCs and GUI, P0 is appropriate for finer resolution (2 and 4 m), and P25 is appropriate for 10 m or coarser resolution urban-scale building footprint identification. Meanwhile, GUI options at 1 m resolution or P0 and P75 are not recommended.

Table 5. Urban-scale mosaic raster data size and identified building and TC footprint area (km^2).

	Probability Density							
	Over 0 (P0)		**Over 25 (P25)**		**Over 50 (P50)**		**Over 75 (P75)**	
	Building	**TC**	**Building**	**TC**	**Building**	**TC**	**Building**	**TC**
1 m (40,615 × 34,000)	16.5	41.0	2.2	25.0	1.2	18.4	0.9	14.4
2 m (20,308 × 17,000)	52.6	111.3	10.2	83.3	5.4	63.1	3.9	49.1
4 m (10,154 × 850)	69.4	132.6	23.8	114.7	13.2	97.6	8.2	79.0
10 m (4062 × 3400)	101.7	164.0	43.7	141.2	22.2	118.3	12.5	88.1
20 m (2031 × 1700)	136.0	179.3	59.3	156.2	26.0	112.7	11.6	59.7
30 m (1354 × 1134)	159.8	181.7	66.8	157.2	23.1	96.2	12.2	32.4

Building footprint area true value zone: 40–100 km^2; tree canopy (TC) footprint area true value zone: 80–160 km^2.

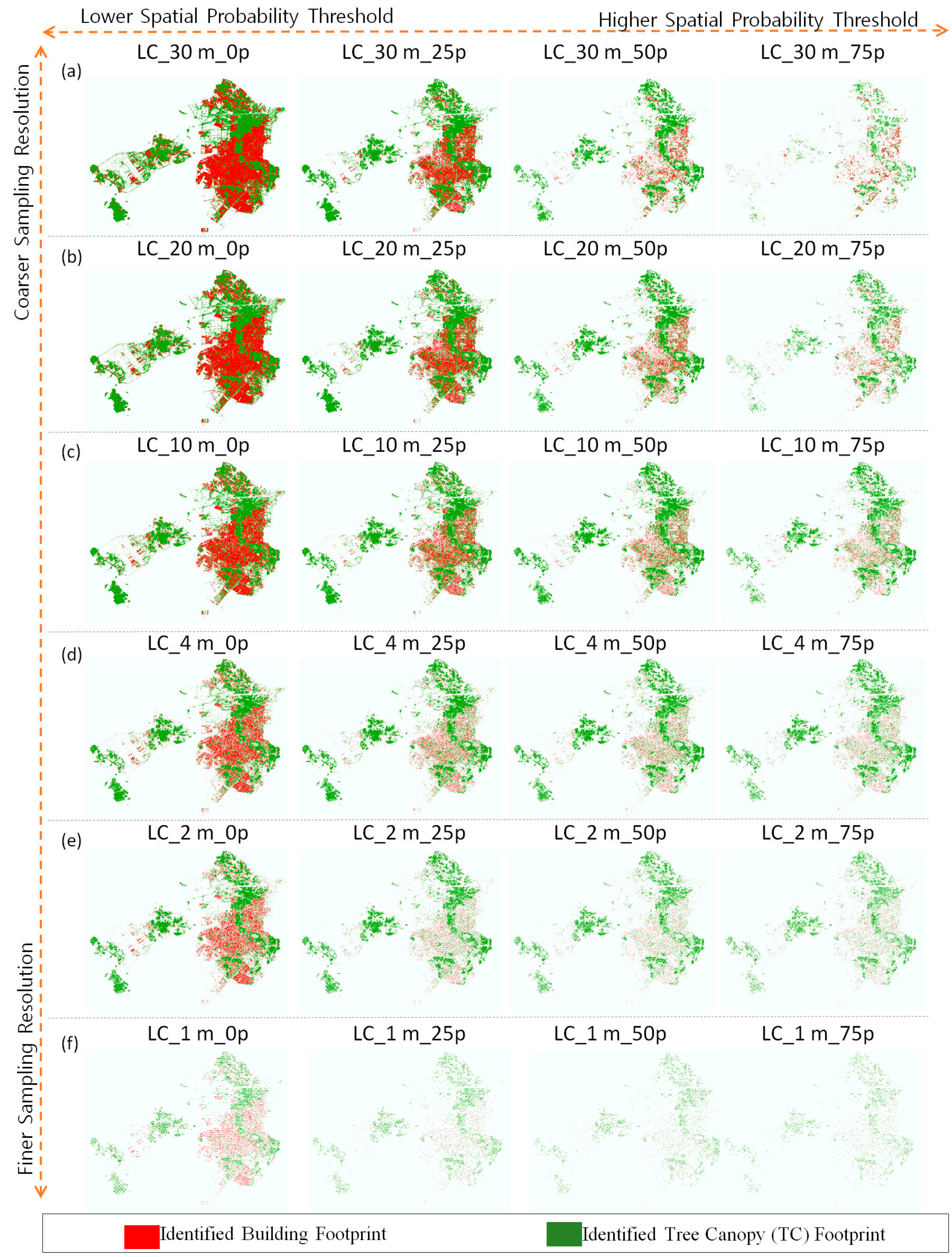

Figure 6. Urban-scale visual comparison of the identified building and tree canopy (TC) footprint generated from the six sampling resolutions (**a**–**f**) 1, 2, 4, 10, 20, and 30 m, respectively, and four different SP thresholds (P0, P25, P50, and P75).

In contrast, many major portions of the urban-scale TC footprint area (km^2) values for P0, P25, and P50 were in the true value zone, although a few were outside (Figure 7b). In the P0 and P25 cases, all values except for 1 m resolution were in the true value zone and were not overestimated with a parabolic curve trend, indicating that the P0 and P25 TC footprint area values were less sensitive to the resolution variation than the building footprint. Underestimation became stronger as the resolution became finer or the SP threshold increased. However, at coarser resolutions (20 and 30 m), the TC footprint area significantly decreased, particularly at higher SP threshold resolutions (P50 and P75). This is primarily due to priority being given to building footprints when footprint competition occurs between the building and TC (Figures 6 and 7); the coarser the resolution applied in the study area, the smaller the TC footprint area return due to the one-sided building footprint allocation priority. That is, the reason for the improvement does not appear to be the increased TC footprint identification accuracy but rather the positive and negative errors offsetting each other. Indeed, the weakness is more apparent when the TC land cover heterogeneity in a cell increases. Hence, caution must be exercised when land cover heterogeneity increases due to coarse cell resolution to prevent TC and other land cover footprint areas from being assigned to building footprints.

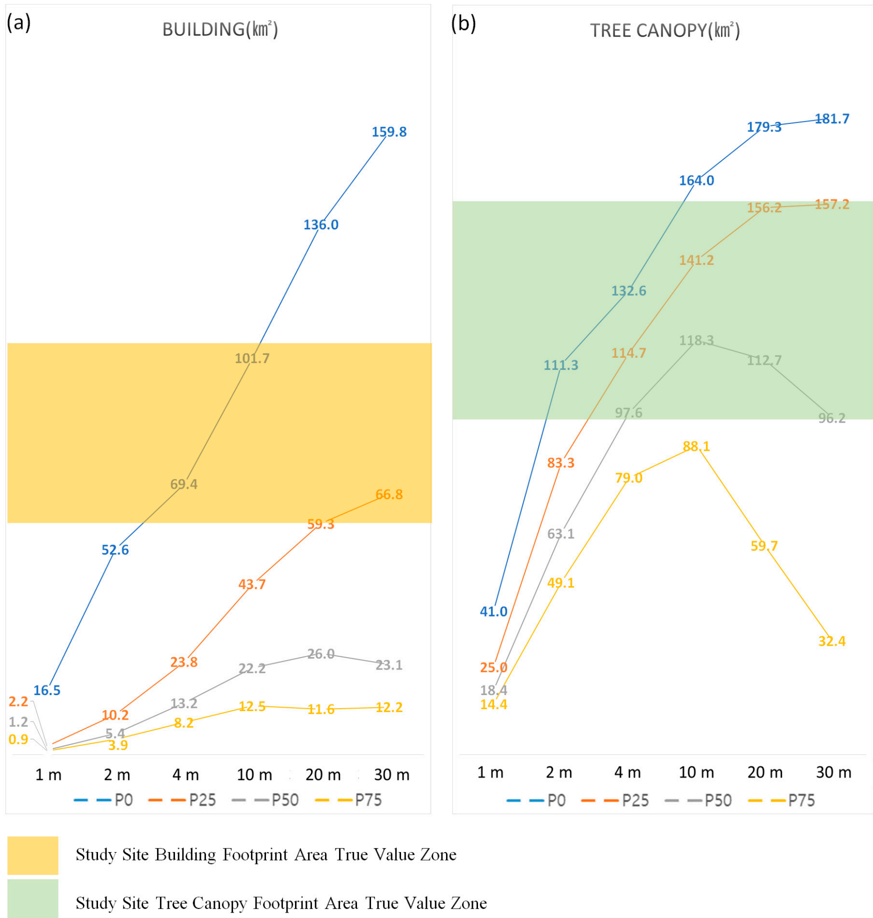

Figure 7. Statistical comparison of the identified urban-scale building and TC footprint area with different resolutions (1, 2, 4, 10, 20, and 30 m) and SP thresholds (P0, P25, P50, and P75). (**a**) Building footprint identified area variance by resolution compared to the true value zone (Yellow; 40–100 km^2). (**b**) Tree canopy identified area variance by resolution compared to the true value zone (Blue; 80–160 km^2).

In comparison with the identified building or TC footprints, the multiresolution urban-scale SVF maps and averaged statistics exhibited considerably more consistent results. However, unlike the identification process, the 750 3DPC file batch required huge storage and a much longer time as the sampling resolution became finer (Table 6). However, post-work, including mosaic or map algebra processing times, did not show significant differences. Four DIF maps were calculated from eight mosaiced SVF maps by applying simple map algebra (Figure 8d), which had different data sizes and were completed in a maximum of 1 h (Table 6). A superficial comparison reveals that the three types of SVF maps (GB, GBH, and DIF) were visually consistent. Despite four different sampling resolutions, the average SVF values for GB, GBH, and DIF were statistically consistent. These visual consistencies were also confirmed by the urban-scale-averaged SVF statistics. As shown in Figure 7 and Table 6, unlike the significant variations among the identified building and TC footprint areas, minimal variations were detected in the mean, maximum, and standard deviation of SVF DIF. The urban-scale SVF–DIF map measures the range of

TC-induced values across the entire study area. According to the resolution variation, the urban-scale mean SVF DIF range was 0.685–0.687, indicating that the difference between the highest and lowest SVF values was small (0.002). This suggests that a resolution of 1–30 m did not significantly alter the SVF maps and values. Unlike LiDAR footprint identification, the SVF value consistency was offset between the positive and negative errors.

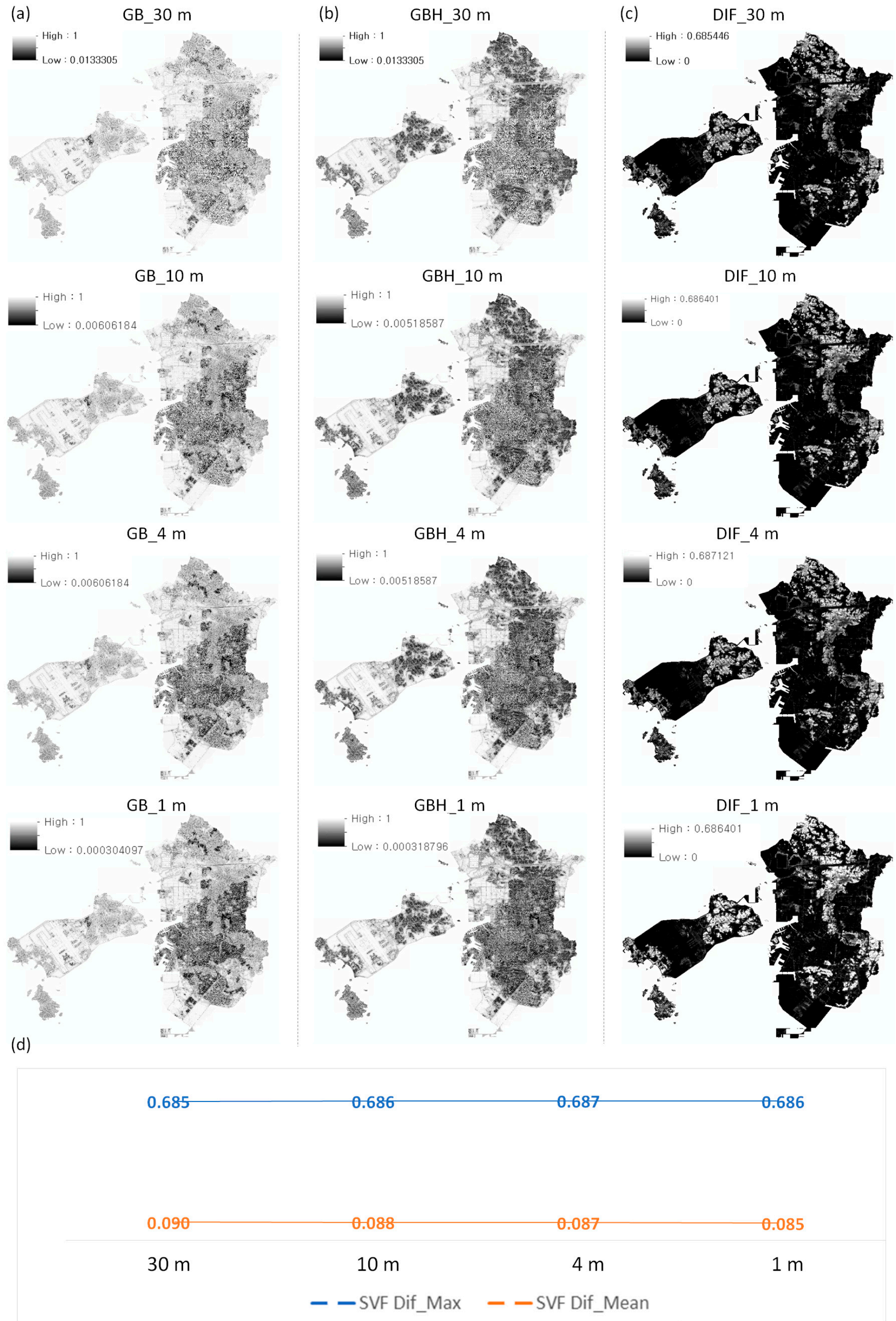

Figure 8. Urban-scale visual and statistical comparisons of the SVF generated from the four sampling resolutions (1, 4, 10, and 30 m). (**a**) TC presence (GB) sky view factor (SVF); (**b**) TC absence (GBH) SVF; (**c**) SVF difference (DIF); (**d**) Statistical comparison of the max and mean values for the SVF DIF.

The primary reasons for the observed visual difference (Figure 6 vs. Figure 8a–c) and statistical difference (Figure 7 vs. Figure 8d) were the number of classified 3DPCs used by search distance types, interactive random point search distance for footprint identification, and maximum search distance for SVF analysis. Footprint identification by interactive random point search distance used a few LiDAR points located in the cell; hence, the SP value was affected by the distribution of the points. However, SVF by maximum search distance used sufficient LiDAR points located inside or outside the cells, making the SVF value more continuous for surrounding cells and less sensitive to resolution variations. For instance, according to the 100 m maximum search distance and the ALS LiDAR acquisition guideline standard (2.5 pt/m^2), the cell center-oriented usable number of 3DPCs was approximately 78,500 points, which made SVF values less sensitive to the resolution variance (1, 4, 10, and 30 m). In contrast, the maximum number of usable points for a 1 m resolution cell SP calculation would be 2.5, and a 30 m resolution cell SP calculation would be 2250, according to the guideline standard. In addition, the density classified as a building or TC was <2.5 pt/m^2. Hence, the finer the grid cell resolution, the fewer usable points for footprint identification. Consequently, the difference in the number of usable points exacerbates the visual and statistical differences.

Table 6. Urban-scale sky view factor (SVF) mosaic raster data size and statistics.

SVF Mosaic	Data Size	Columns × Rows	Min	Max	Mean	Std
GBH_30 m	5.86 MB	1354 × 1134	0.013	1.000	0.739	0.218
GBH_10 m	52.68 MB	4062 × 3400	0.005	1.000	0.712	0.215
GBH_4 m	329.24 MB	10,154 × 8500	0.005	1.000	0.693	0.215
GBH_1 m	5.14 GB	40,615 × 34,000	0.000	1.000	0.679	0.213
GB_30 m	5.86 MB	1354 × 1134	0.013	1.000	0.829	0.179
GB_10 m	52.68 MB	4062 × 3400	0.006	1.000	0.800	0.178
GB_4 m	329.24 MB	10,154 × 8500	0.006	1.000	0.781	0.182
GB_1 m	5.14 GB	40,615 × 34,000	0.000	1.000	0.765	0.185
DIF_30 m	5.86 MB	1354 × 1134	0.000	0.685	0.090	0.125
DIF_10 m	52.68 MB	4062 × 3400	0.000	0.686	0.088	0.122
DIF_4 m	329.24 MB	10,154 × 8500	0.000	0.687	0.087	0.121
DIF_1 m	5.14 GB	40,615 × 34,000	0.000	0.686	0.085	0.119

A visually magnified check focusing on Incheon Central Park (Figure 9) and an in situ site survey (Figure 10) showed the abovementioned differences, as well as more complicated issues during the proposed method comparison with the in situ survey measurement. That is, applying a coarser resolution increased the aboveground feature footprint area (>2 m). A building or TC footprint encroached and occupied an in situ footprint of ground surface land cover types, such as water, grassland, barren land, and transportation (road). The identified building accession footprint occupation in the case of a very low SP (0P) was outstanding due to the coarser resolution (Figure 9a). With low SP and coarse resolution, building footprints significantly encroached on the ground surface feature footprints and TC footprints, which produced a parabolic curve trend (Figure 7b). A one-sided rule that assigns building footprints a higher priority than TC or other ground surface footprints will induce unbalanced and intolerable land cover areal proportions, especially coarser resolutions, such as in the 30 m case in this study. However, we also found that applying a finer resolution forced the building footprint to abandon over-occupied space. As the study area was divided into finer cell spaces, when the resolution was extremely fine (e.g., 1 m or sub-meter), the space in many cells registered as building footprints under coarse resolution was mostly recategorized as empty or TC footprint space (Figure 9a). The extremely fine sampling resolution-induced issue was also observed in the SVF analysis due to the lack of building-class 3DPCs. However, the associated significance was much lower than that of footprint identification. Hence, as an ALS-based solution, more densely classified building 3DPCs are required for finer-resolution building footprint identification. Accordingly, the ALS survey should undergo a lower altitude flight to obtain denser LiDAR 3DPCs. As shown in the Incheon Culture & Art Center vertical wall-sided footprint (Figure 9a,c(1)), which had relatively dense building class points, the space building footprints were relatively robust by high SP and resolution variation.

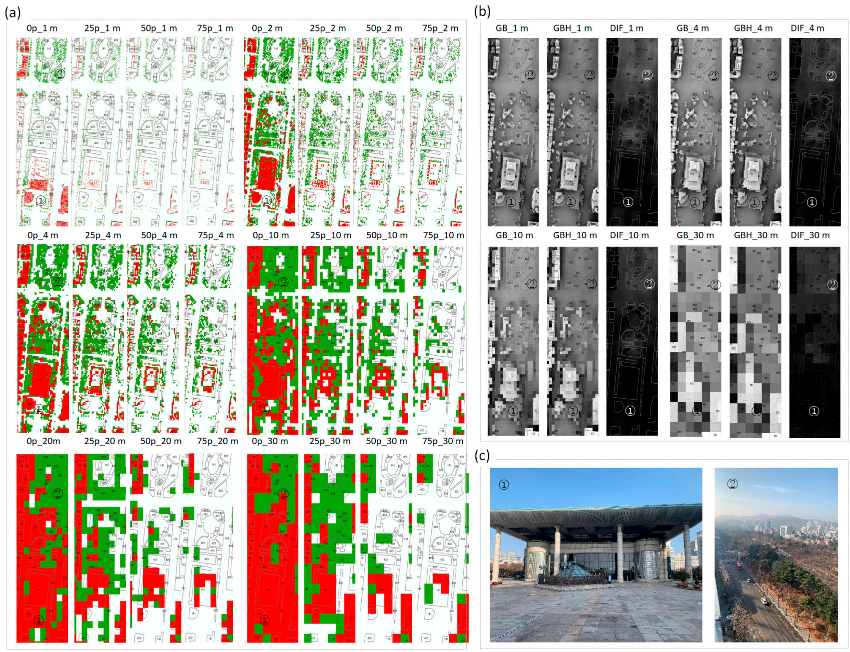

Figure 9. Incheon Central Park magnified visual comparison of the identified building and TC footprints and SVF. (**a**) Six resolutions (1, 2, 4, 10, 20, and 30 m) and four SP thresholds (P0, P25, P50, and P75). (**b**) Four resolutions (1, 4, 10, and 30 m) and three analysis types (GB, GBH, and DIF). (**c**) In situ photographs taken from Incheon Culture & Art Center (1) and Incheon Central Park tree canopy belt (2).

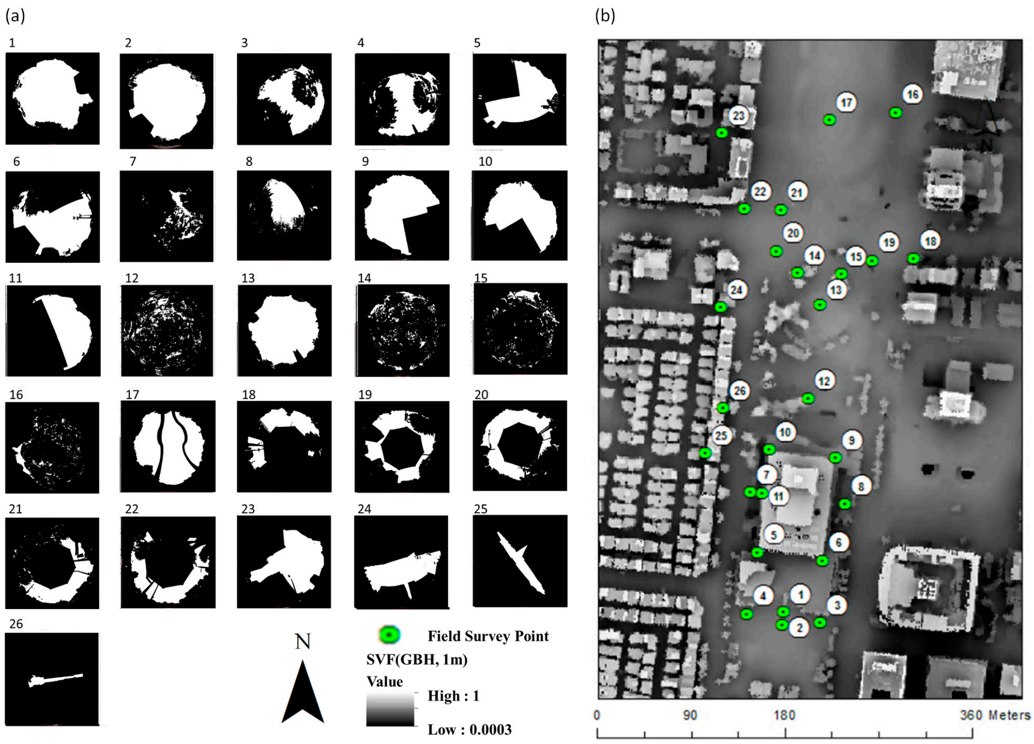

Figure 10. Point-based in situ location SVF value comparison (fish-eye photography vs. LiDAR 3DPC). (**a**) The white area in 26 black-and-white images represents each sky view area from the location. (**b**) Overlay of the 26 sites on a LiDAR SVF analysis map (GBH, 1m).

In contrast, a magnified image of the SVF (GB, GBH, DIF) spatial distribution in and around the Incheon Culture & Art Center showed strong visual consistency despite the significant resolution variations. Nevertheless, differences were apparent between statistical SVF reliability and place-based SVF accuracy. For instance, it is difficult to distinguish a small gap between small buildings in a 2 m resolution SVF map; meanwhile, a resolution coarser than 10 m distorts the original appearance of small or medium size buildings. However, constant or similar visual contexts were maintained across the resolution variation. The analysis of additional TC effects on SVF requires more consideration. The brighter belt area of SVF DIF (Figure 9b) indicates the additional sky view area encroaching due to the TC, which is an important urban setting design component for the screen-level urban climate and human health [5,35]. The SVF DIF distribution pattern was spatially continuous in comparison with the discrete footprint distribution, which can be useful for green axis planning.

The data collected during summer days in the July 2023 field survey provide verification of the LiDAR SVF (Figure 9b GBH_1m), as well as data regarding how large urban canopies impact urban microclimate attributes. As shown in Figure 10 and Table 7, the 26 in situ locations in real urban settings were more complex than digitized virtual urban settings, resulting in a difference in measurements between fish-eye SVF and LiDAR SVF (GBH, 1 m). Generally, the averaged SVF difference mean was small (0.03), while variations in the fish-eye SVF values were relatively higher than point-based GBH SVF values (Figure 11a). This was due to the fish-eye images capturing real sky areas in detail and many urban furniture and features taller than 0.9 m. Meanwhile, in the captured point-based sky view area and obstacle area, street furniture, low vegetation, and temporary obstacles shorter than 2 m are excluded.

Table 7. In situ survey site SVF comparison (fish-eye photography vs. LiDAR 3DPC (GBH. 1 m)) and measured microclimate attributes.

No	SVF			TA (%)	RH (%)	WBGT (%)	Surface Temp. (°C)			Material Type	Shadow /Sunlit	Canopy Type	Zone Code
	Fisheye	GBH	Diff				SATO	Bosh	FLIR				
1	0.83	0.51	0.24	34.6	36.9	30.2	45.6	57.2	55.9	wood	sunlit	open	UQA430
2	0.9	0.56	0.13	34.6	42.6	32.6	45.3	42.3	44.3	granite	sunlit	open	UQA430
3	0.47	0.42	−0.04	33.2	45.4	29.9	44.2	30.8	31.2	granite	shadow	tree	UQA430
4	0.49	0.46	−0.1	32.3	48.5	28.6	28.8	29.6	29.2	granite	shadow	tree	UQA430
5	0.61	0.36	−0.26	36.3	43.8	29.7	40.2	40.4	38.6	granite	sunlit	open	UQA430
6	0.62	0.48	−0.21	34.2	42.1	29.6	42.6	41.3	39.6	granite	sunlit	open	UQA430
7	0.11	0.34	0.32	31.8	45.8	26.9	35.4	30.4	29.1	granite	shadow	tree	UQA430
8	0.35	0.41	0.34	32.8	44.6	29.2	42.6	28.3	26.2	granite	shadow	tree	UQA430
9	0.74	0.55	0.25	34.6	36.8	27.1	37.1	41.4	39.5	granite	sunlit	open	UQA430
10	0.66	0.48	0.14	32.2	42.1	27.9	40.3	24.5	23.3	granite	sunlit	open	UQA430
11	0.45	0.46	0.19	31.4	44.4	26.1	34.3	27.5	26.0	granite	shadow	open	UQA430
12	0.13	0.51	0.18	29.7	48.5	24.9	32.2	26.6	23.8	loam	shadow	tree	UQA430
13	0.86	0.58	−0.01	33.2	41.0	29.5	43.8	40.7	50.0	granite	sunlit	open	UQA430
14	0.08	0.43	0.28	30.8	45.6	26.8	36.8	24.9	25.1	loam	shadow	tree	UQA430
15	0.05	0.46	0.18	31.6	46.8	26.7	34.4	24.8	24.5	loam	shadow	tree	UQA430
16	0.06	0.43	−0.24	32	39.6	27.3	38.7	29.1	28.0	cement	shadow	Tree	UQA430
17	0.78	0.6	−0.24	39.6	32.8	33.6	50.9	45.7	46.0	granite	sunlit	open	UQA430
18	0.19	0.4	−0.32	32.3	41.4	26.2	34.2	30.9	31.2	granite	shadow	parasol	UQA220
19	0.29	0.53	0.05	32.8	40.0	26.5	34.7	35.1	34.0	granite	shadow	parasol	UQA430
20	0.32	0.56	0.03	31.2	44.5	26.8	36.3	35.8	35.0	granite	shadow	parasol	UQA430
21	0.21	0.53	−0.23	31.7	42.2	26.1	35.7	33.5	32.0	granite	shadow	parasol	UQA430
22	0.21	0.47	−0.06	32.2	44.0	27.0	35.7	35.0	34.4	granite	shadow	parasol	UQA130
23	0.58	0.34	−0.38	33.2	40.8	27.8	37.4	45.3	45.7	asphalt	sunlit	open	UQA122
24	0.43	0.3	−0.35	33.6	41.2	27.9	36.9	48.1	47.5	asphalt	sunlit	open	UQA122
25	0.17	0.21	−0.41	34.3	38.3	28.7	35.6	35.1	36.2	cement	sunlit	open	UQA130
26	0.07	0.17	−0.37	32.5	45.6	27.3	35.9	28.8	28.3	cement	shadow	open	UQA130
Mean	0.41	0.44	−0.03	33.0	42.5	28.1	38.3	35.1	34.3	-	-	-	-

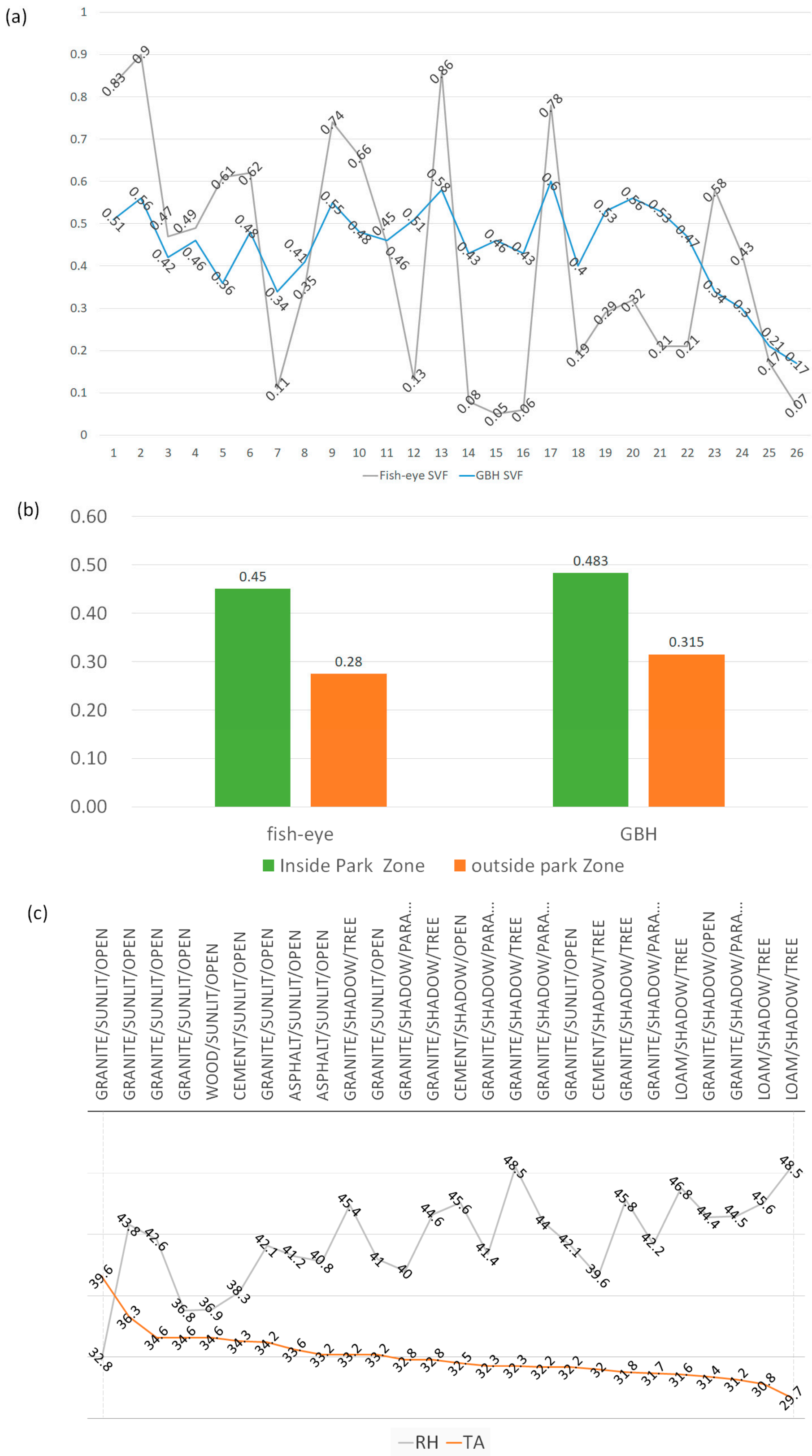

Figure 11. In situ survey site SVF and microclimate. (**a**) A 26-point SVF value comparison (fish-eye photography vs. LiDAR 3DPC (GBH. 1 m)). (**b**) Land-use-based mean SVF value comparison (inside park zone vs. outside park zone). (**c**) Measured air temperature (AT) and relative humidity (RH) variation according to the sunlight environment, ground material, and urban canopy.

As in many other studies, the link between land use plans and sky view area is demonstrated in Figure 10. Building setting patterns caused by land use zone designation differentiates the SVF values. The SVF mean of the Urban/Green/ Natural zone (UQA430) appeared twice bigger than the outside park area (UQA122, UQA130, UQA220) SVF mean (Figure 11b). Moreover, several public buildings in Inchon central park and east side high-rise buildings encroach on the sky view area. However, they have minimal effects on the Urban/Green/Natural zone (park area) SVF. In contrast, the TC significantly encroaches on the SVF in the park area. Although the TC area is not abundant outside the park area, interestingly, foldable solar parasols exhibit a canopy role in the open street. According to the solar path drawn from the SOLWEIG1D model, parasols can typically cast shade in the central area from 10:00 to 15:00; the shorter the parasol height, the longer the time to cast the shade (Figure 4a).

The field survey demonstrated that many other factors can also affect in situ observations. As shown in Table 7 and Figure 11, the measured microclimate attribute values imply that multiple interactions can occur between weather and urban settings. Although the measurement instruments had low accuracy, AT and RH values reasonably varied according to composite variations in the material type, shade/sunlit, and canopy type, reasonably (Figure 11c). For instance, the sunlit/granite/open area showed the highest AT (39.6 °C) and lowest RH (32.8%), whereas the shade/loam/tree area had the lowest AT (29.7 °C) and highest RH (48.5%); other microclimate variations were distributed in between. Moreover, various unmeasured factors in the survey could affect the measurement results. For instance, during the short ~2 h field measurement period, the wind speed and cloud cover changed significantly, which could have affected measured microclimate attribute values. Nevertheless, the importance of the urban natural and artificial canopies is reflected in the measured values, highlighting their role in in situ urban microclimate.

4. Discussion

The integrated urban-scale land cover footprint and SVF analysis maps from LiDAR 3DPC exhibited various limitations and research imperfections. However, they also proved that evaluating a climatically resilient and adaptive urban setting is feasible. Moreover, the results of this study support the application of big data, such as LiDAR, in urban-scale planning approaches. Hence, constructing a wider urban scale with improved resolving power is feasible to generate and manage big data. Nevertheless, the proposed methodology and results are immature and further research is required to address the remaining challenges.

4.1. Applicability for Urban-Scale Studies

4.1.1. Institutional Land Cover or Land Use Map Update

The proposed method can be applied for institutional land cover and land use map updates. To date, land use and land cover maps have commonly been used as major datasets for urban-scale studies [3,36]. Over decades of urbanization, buildings have been continuously constructed or destroyed, vertically changing urban settings with TC. Urban trees in streets and parks show greater variability than buildings due to their biological growth and the relative ease with which they can be removed. Accordingly, street trees are occasionally regarded as urban furniture. Land cover or land use map updates require information about building and TC footprints and their vertical and versatile attributes. LiDAR 3DPCs can support these updates.

Collaboration with models will support land use plans that can access and explore future land cover changes [36]. In the Republic of Korea, the best available, quality-controlled, large-scale, and detailed institutional land cover map is provided by ME (L3), and institutional land use maps are provided by MOCT (Table 1); however, these do not include urban-scale data but rather national-scale data. Meanwhile, the building and TC footprints (2 m resolution) can support land cover (L3) updates; areal or vertical attributes are useful to update auxiliaries (Figure 12 and Table 8). For instance, when a transition from deciduous forest land cover to multifamily units occurs, the resulting change could potentially be detected from the time series composite of building and land cover footprints. Current institutional land cover has been updated from the visual interpretation and manual digitization using 1 m or sub-meter resolution satellite remote sensing, and ME announced a plan to further update these resources. However, the associated manual work will require a significant amount of time to complete. Hence, a foundation for advanced solutions is also needed. Martins et al. [37] suggested that advancements in technology, such as machine learning, would enable more precise and accurate urban setting mapping and updates. This could enhance LiDAR 3DPC application for context interpretation and decision support.

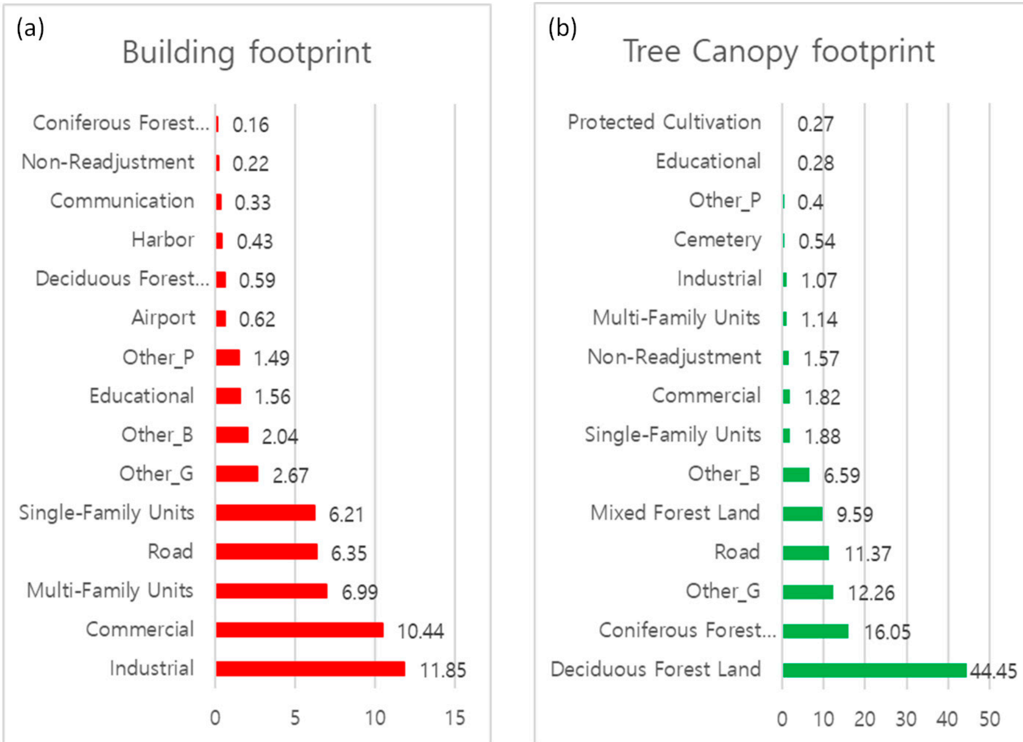

Figure 12. The top 15 ME land covers (L3) and corresponding (**a**) building footprint area (km^2) and (**b**) TC cover footprint area (km^2).

Table 8. Ministry of Environment (ME) land cover (L3) area and its corresponding building and the TC footprint area.

L3 Name	ME Land Cover		LiDAR 3DPC			
	L3 Code	L3 Area	Building (km^2)	Building/ L3 Area (%)	Tree (km^2)	Tree/ L3 Area (%)
Single-Family Units	111	10.1	6.21	61.49	1.88	18.61
Multi-Family Units	112	10.58	6.99	13.30	1.14	10.78
Industrial	121	15.23	11.85	22.50	1.07	7.03
Commercial	131	15.92	10.44	19.80	1.82	11.43
Complexes	132	0.04	0.01	0.00	0	0.00
Communication	141	2.08	0.33	0.60	0.23	11.06
Airport	151	0.7	0.62	1.20	0.01	1.43
Harbor	152	3.73	0.43	0.80	0.15	4.02
Railroad	153	1.1	0.04	0.10	0.06	5.45
Road	154	107.54	6.35	12.10	11.37	10.57
Other_T	155	0.05	0.02	0.00	0	0.00
Environmental	161	0.5	0.12	0.20	0.04	8.00

Table 8. *Cont.*

L3 Name	L3 Code	ME Land Cover L3 Area	Building (km^2)	Building/ L3 Area (%)	LiDAR 3DPC Tree (km^2)	Tree/ L3 Area (%)
Educational	162	2.42	1.56	3.00	0.28	11.57
Other_P	163	5.72	1.49	2.80	0.4	6.99
Readjustment	211	8.64	0	0.00	0.01	0.12
Non-Readjustment	212	9.43	0.01	0.00	0.05	0.53
Readjustment	221	1.42	0	0.00	0.03	2.11
Non-Readjustment	222	19.56	0.22	0.40	1.57	8.03
Protected Cultivation	231	2.83	0.1	0.20	0.27	9.54
Orchard	241	1.15	0.03	0.10	0.22	19.13
Ranch or Farm	251	0.2	0.06	0.10	0.04	20.00
Other_C	252	1.27	0.02	0.00	0.24	18.90
Deciduous Forest Land	311	51.95	0.59	1.10	44.45	85.56
Coniferous Forest Land	321	19.01	0.16	0.30	16.05	84.43
Mixed Forest Land	331	11.98	0.12	0.20	9.59	80.05
Natural Grassland	411	0.86	0.01	0.00	0.18	20.93
Golf Course	421	4.25	0	0.00	0.11	2.59
Cemetery	422	2.86	0.01	0.00	0.54	18.88
Other_G	423	65.96	2.67	5.10	12.26	18.59
Inland Wetland (Vegetation)	511	15.11	0.03	0.10	0.21	1.39
Tidal Flat	521	7.68	0.01	0.00	0.01	0.13
Salt Field	522	0.77	0	0.00	0	0.00
Beach	611	1.23	0	0.00	0.05	4.07
Riverside	612	0.26	0	0.00	0	0.00
Exposed Rock	613	0.39	0	0.00	0.09	23.08
Quarry	621	0.2	0	0.00	0.01	5.00
Playground	622	2.34	0.04	0.10	0.11	4.70
Other_B	623	78.56	2.04	3.90	6.59	8.39
Stream and Canal	711	5.33	0	0.00	0.07	1.31
Lake and Reservoir	712	8.44	0.01	0.00	0.03	0.36
Seawater	721	5.74	0.01	0.00	0.01	0.00
Total	-	-	52.64	-	111.27	-

4.1.2. Enhanced Urban-Scale Land Use Management

Fundamentally, one of the goals of urban planning is to optimize the reallocation of complex urban settings. In this context, while diagnosing the current situation is important, planning future urban settings typically garners more attention and is evaluated via the current institutional land use map. Traditional land use maps primarily focus on zoning for buildings related to residential planning. However, global climate change increasingly motivates concerns about other urban settings, including the tree canopy. Currently, urban environment assessments are based on changes in the institutional land cover. Meanwhile, ultimately, building and TC footprints and their functional information will be required to make land use designation decisions. Accordingly, numerous essential indicators of sustainable urban settings will be introduced, requiring the implementation of various auxiliary indicators, including LiDAR. Hence, developed urban-scale high-resolution LiDAR footprints and SVF analysis must be applied for Urban/Green/Natural zone (UQA430) planning.

As shown in Figure 13 and Table 9, the Urban/Green/Natural zone has outstanding coverage in the study area (55.65 km^2), and its additional SVF DIF due to the presence of the TC in the urban environment is considerably good (SVF DIF: 0.10); this can be applied as an auxiliary indicator to assess its heat island mitigation function (Figure 13c). In contrast, the Urban/Green/Conservation zone (UQA410) has outstanding SVF DIF (0.24), and its coverage in the study area is considerably good (10.96 km^2). The information derived from the raster map overlay using the land use zone (Figure 13a) and SVF DIF (Figure 13b) is useful and expandable. However, it would take more time and effort to support more efficient land use management. LiDAR 3DPC-based analysis methods and applications are emerging; however, other novel strategies are needed to optimize the balance between individual interest and entire land use sustainability. Enhanced urban-scale land use applications will support the development of advanced strategies to ensure urban settings are spatially balanced and functionally optimized.

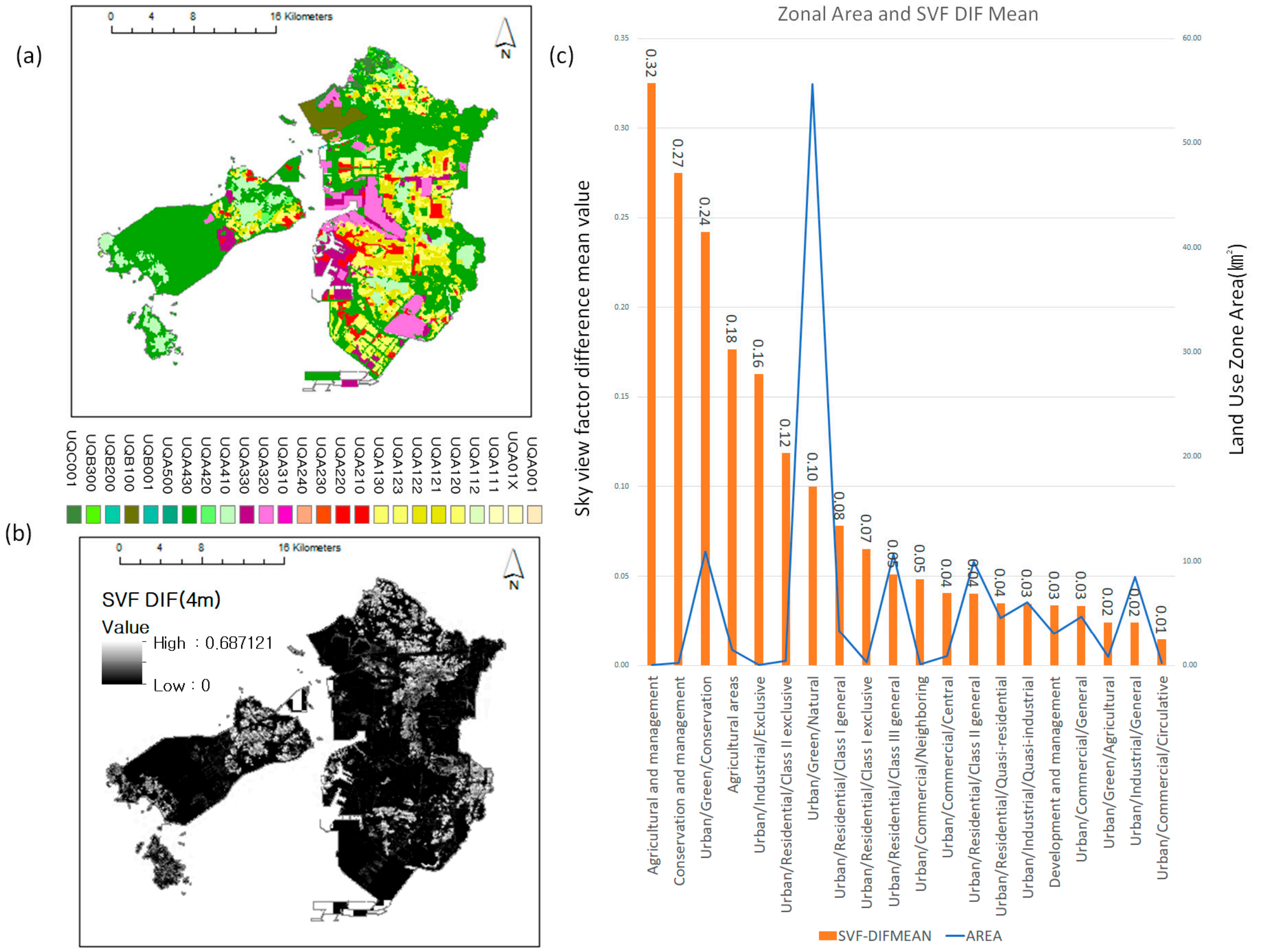

Figure 13. Land use and SVF DIF zonal overlay and zonal mean SVF DIF values of each land use zone type. (**a**) Land use of the study area. (**b**) SVF DIF of the study area. (**c**) Land use area of the study site (km^2; orange bar) and SVF DIF zonal mean value of each land use zone type (blue lines).

4.1.3. Digital Twin (DT)

Urban settings have changed rapidly since the birth of the city and will continue to evolve more quickly. However, due to climate change acceleration, city members' demands for rapidly, spatially, and functionally transitioning into an urban setting have also increased. Hence, a digital twin (DT) is comprehensively discussed for the first time to reduce the occurrence risk of a rapid transformation of urban settings. DT is defined as a virtual model of national infrastructure, which monitors infrastructure in real-time and has predictive capabilities [38].

The alterability of urban-scale settings significantly depends on the monitoring of complexities, such as vertical variation. The need for building or TC DTs will increase with advances in urban surveying technologies [20,31]. However, currently being developed, DTs for buildings and TC are insufficient; data mismatch cases are abundant up to now. For instance, building footprints and areas is fundamental information for urban monitoring, but many maps provide different values owing to the different surveying periods, classification rules, and applications of mapping workbenches. As seen in Table 10, the map overlay comparison between the building footprint of the digital map (1/5000, 48.68 km^2) and the LiDAR 3DPC-based building footprint (2 m, P0, 52.6 km^2) showed 72.1% (35.08 km^2)

locational matches, but 28.1% (13.6 km^2) of the digital map footprint area did not have a building footprint. A similar mismatch was derived from the opposite.

Table 9. SVF difference (DIF) zonal mean values of each land use zone type.

Code	Land Use Zone Name	Count	Area (km^2)	SVF Dif
UQB200	Agricultural and management	10,717	0.04	0.32
UQB300	Conservation and management	62,622	0.25	0.27
UQA410	Urban/Green/Conservation	2,740,837	10.96	0.24
UQC001	Agricultural areas	370,061	1.48	0.18
UQA310	Urban/Industrial/Exclusive	4210	0.02	0.16
UQA112	Urban/Residential/Class II exclusive	110,745	0.44	0.12
UQA430	Urban/Green/Natural	13,911,797	55.65	0.1
UQA121	Urban/Residential/Class I general	833,660	3.33	0.08
UQA111	Urban/Residential/Class I exclusive	73,533	0.29	0.07
UQA123	Urban/Residential/Class III general	2,663,943	10.66	0.05
UQA230	Urban/Commercial/Neighboring	23,645	0.09	0.05
UQA210	Urban/Commercial/Central	218,788	0.88	0.04
UQA122	Urban/Residential/Class II general	2,482,510	9.93	0.04
UQA130	Urban/Residential/Quasi-residential	1,142,661	4.57	0.04
UQA330	Urban/Industrial/Quasi-industrial	1,525,095	6.1	0.03
UQB100	Development and management	768,796	3.08	0.03
UQA220	Urban/Commercial/General	1,182,845	4.73	0.03
UQA420	Urban/Green/Agricultural	200,291	0.8	0.02
UQA320	Urban/Industrial/General	2,131,985	8.53	0.02
UQA240	Urban/Commercial/Circulative	65,194	0.26	0.01

Table 10. Digital map building footprint and LiDAR-driven building footprint (2 m, P0) map overlay comparison.

	LiDAR 3DPC-Based Building Footprint				LiDAR 3DPC
NGII Digital Map (NCA_B0010000) Building Type (KIND)	Code	Count ea (%)	Sum Area [km^2 (%)]	Mean Area [m^3]	Identified [km^2/%]
Unclassified	BDK000	13,015 (4.8)	1.22 (2.5)	93.5	0.75 (61.4)
Single-family house	BDK001	77,004 (28.2)	6.00 (12.3)	77.9	4.49 (74.8)
Townhouse	BDK002	26,538 (9.7)	4.16 (8.5)	156.7	2.93 (70.4)
Apartment	BDK003	7980 (2.9)	4.90 (10.1)	613.9	3.60 (73.6)
Non-residential	BDK004	99,979 (36.6)	29.24 (60.1)	292.5	21.88 (74.8)
Wall-less/Open	BDK005	38,951 (14.3)	2.21 (4.5)	56.7	1.04 (47.2)
Greenhouse	BDK006	1069 (0.4)	0.16 (0.3)	146.7	0.03 (19.1)
Under construction	BDK007	214 (0.1)	0.29 (0.6)	1331.8	0.08 (27.1)
Temporary	BDK008	8495 (3.1)	0.51 (1.1)	60.5	0.28 (54.8)
Total		273,245 (100.0)	48.68 (100.0)		35.08 (72.1)

In Korea, a plan to support the national spatial data-based DT (NDT) has been comprehensively discussed, leading to the implementation of NDT policy-based projects. From the perspective of urban settings, spatial information development has considered smart cities (Figure 12a). Hence, the NGII survey program has been constructing annual aerial photo orthoimage databases (DBs) of the entire country as a data-supporting foundation to realize NDT. Twenty years ago, the expected update cycle for building information on digital maps was 10 y, while the tree update cycle has not yet been discussed. However, based on the LiDAR ALS experience from 2002 to 2021 (Figure 14b), the NGII launched a new program to generate airborne LiDAR 3DPC data covering the entire urban area every 2 y, the southern regions for odd years and the northern regions for even years (Figure 14c). Indeed, many urban models are dependent on the NDT data. Recently, thermal environment analyses and evaluation studies have considered DT platforms and models to support climate change adaptation and mitigation [20]. Many models use SVF as a spatial attribute for model enhancement [35,39,40] by applying it as a spatial data source for urban-scale thermal environment analysis or assessment. It is currently being utilized to develop various urban climate analysis models, such as perceived temperature. Hence, seamless SP and SVF calculations will accelerate urban setting DT platforms. Buildings, TC, and artificial canopies, such as parasols, are important urban setting components for DT-based planning or risk management (Figure 14d).

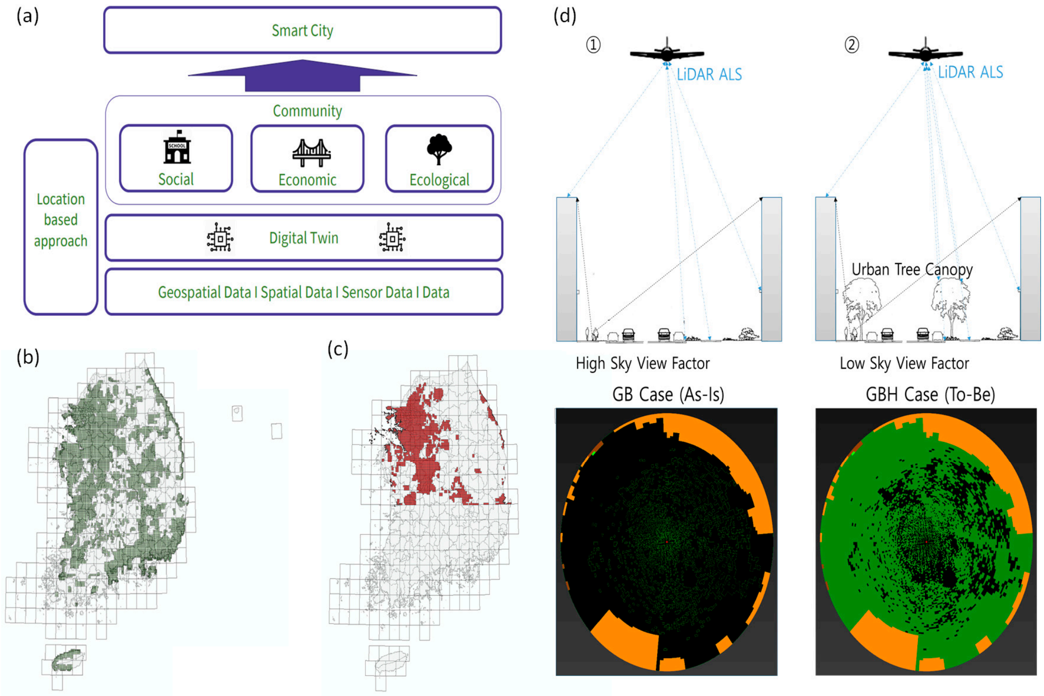

Figure 14. Geospatial data-based digital twin (DT), Smart City vision, and proposed works based on the ALS LiDAR Survey DT plan of NGII in Korea. (**a**) DT and Smart City (Source: Kedar [41]). (**b**) ALS LiDAR DB constructed an urban area from 2002 to 2021 (green). (**c**) NDT supporting ALS LiDAR DB constructed urban area in 2022 (red). (**d**) City-based urban-scale building and tree canopy identification and SVF analysis using DT LiDAR 3DPC.

4.2. Challenges and Further Works

4.2.1. Applying Classified LiDAR 3DPCs to the NDT

Geospatial data, technologies, and services are critical components of a nation's digital infrastructure, including low-carbon cities [42,43]. Similar to the Federal Geographic Data Committee in the USA, the 7th Korea national spatial data infrastructure (NSDI) plan, which will be published soon, primarily focuses on the NDT. Unfortunately, the discussion on LiDAR remote sensing has not been highlighted in the NSDI plan and will proceed as a sub-plan for the digital elevation model (DEM) update. LiDAR ALS is a component of the 3D spatial data infrastructure mission, while DTs in urban settings are not included. This is primarily due to the difficulty of QA/QC and the budget; labor devoted to manual corrections typically requires 25% or more of the total budget. According to O'Neil-Dunne et al. [44], these types of mapping projects, covering huge urban areas, require considerable effort and budgets ranging from tens to hundreds of billions. Hence, LiDAR 3DPC application-based urban setting DTs should consider urban society demands, and benefit/cost (B/C) efficiency should be addressed in the next NSDI plan. As a future direction for LiDAR DT, LiDAR application processing automation is needed. Instructional guidelines or a user guide should be prepared similar to that provided by the UK [45] for LiDAR 3DPC application-based urban setting DTs.

4.2.2. GUI as a General and Global Application

The GUI results highlighted future works for general and global use, as follows:

(1) Cell-based footprint identification improvement for various urban settings. The traditional mapping and modeling process selects and determines only one by generalization [36,46,47]. Hence, building and TC footprints identified by uniform thresholds induce a significant mismatch (Figure 9). The coarser the resolution, the more heterogeneous urban settings are expected in the cell. Uniform thresholds will increase the uncertainty of the identification. If cell resolution is fine, less uncertainty is expected as urban settings in the cell are relatively monotonous [48]. In situ survey results revealed that urban settings are complex and heterogeneous. Hence, inadequate in situ urban settings reflection could lead to inadequate evaluation and management directions. From this perspective, the current grid allows only one type of identification per cell and is no longer sustainable. Traditional deterministic 2D land cover mapping systems will no longer apply to NDT, and eventually, advanced land use models [36] will emerge. Recent LiDAR 3DPC studies have pioneered a new mapping system with the goal of fully automated processing based on big data and machine learning. In addition, AI-related research is of interest in remote sensing [49,50]. A fundamentally improved approach is needed for cell-based urban settings exploration and selection (identification).

(2) SVF analysis improvement. An et al. [13] developed a LiDAR 3DPC application method by manipulative definition for experimental use; however, it requires further improvement for advanced urban setting approaches. As seen in Figure 14d, a one-sided rule that assigns building footprints higher priority than TC footprints is also applied to the virtual hemisphere. Although the in situ TC was closer to the observation point than the building, when overlap occurred, the building prevailed and was virtually fronted. Various methods have been proposed as solutions, including a 3D model-based SVF analysis. In this regard, the algorithm for quantifying the interactions between buildings and TC must be further improved as urban buildings become more vertical and trees grow densely in various locations around them. From this perspective, improvement to evaluate the interrelation among urban settings is urgent.

(3) GUI improvement. As shown in Figures 6, 8 and 9, urban-scale footprint maps, arrayed as a series of image spreadsheets, are expressed with different visual information. These do not have interactive functions but play the same role [22,51,52]. The contribution of the visual comparison of different alternatives is evident. Unifying the view size with an automated array and common viewpoints allows users to compare the results driven by their intended choices. Returning to the proposed motivation, knowing where something happens can be critically important to obtaining urban setting knowledge, ranging from form to function. Immersive visualization and virtual reality can facilitate next-generation urban settings development collaboration [44]. The advanced GUI will expand the user experience and enhance visual analytics capabilities [53].

5. Conclusions

Urbanization continuously transforms vertical urban settings and sky-view areas; thus, evaluating building and TC footprints will continue to garner interest in urban-scale and fine-resolution remote sensing studies. Identification and analysis of urban-scale virtual settings based on comprehensive knowledge development, scientific data-driven urban setting optimization, and balanced planning and implementation are feasible. This study proposed a LiDAR remote sensing application approach, which was validated experimentally to identify the associated challenges and limitations. Consequently, the following conclusions were established:

First, LiDAR remote sensing-based data are utilized for urban-scale building and TC footprint identification. Second, an SVF analysis, which produces results with finer resolutions and wide urban coverage, is performed.

Finally, the proposed method is still in its infancy, and further development via DT technology should be considered for achieving more advanced urban setting management. DT of Buildings, TC, and other artificial canopies, such as parasols, should be promoted to lessen the risks associated with rapid and unknown urban setting transitions.

Funding: This study was supported by a 2020-MOIS35-001 (RS-2020-ND629021) of Policy-linked Technology Development Program on Natural Disaster Prevention and Mitigation funded by Ministry of Interior and Safety (MOIS, Korea).

Conflicts of Interest: The authors declare no conflict of interest. The funders had no role in the design of the study; in the collection, analyses, or interpretation of data; in the writing of the manuscript; or in the decision to publish the results.

References

1. Fineschi, S.; Loreto, F. A survey of multiple interactions between plants and the urban environment. *Front. For. Glob. Chang.* **2020**, *3*, 30. [CrossRef]
2. Semeraro, T.; Scarano, A.; Buccolieri, R.; Santino, A.; Aarrevaara, E. Planning of urban green spaces: An ecological perspective on human benefits. *Land* **2021**, *10*, 105. [CrossRef]
3. Pan, T.; Kuang, W.; Pan, R.; Niu, Z.; Dou, Y. Hierarchical Urban Land Mappings and Their Distribution with Physical Medium Environments Using Time Series of Land Resource Images in Beijing, China (1981–2021). *Remote Sens.* **2022**, *14*, 580. [CrossRef]
4. Bolund, P.; Hunhammar, S. Ecosystem services in urban areas. *Ecol. Econ.* **1999**, *29*, 293–301. [CrossRef]
5. Kim, K.R.; Yi, C.; Lee, J.S.; Meier, F.; Jänicke, B.; Fehrenbach, U.; Scherer, D. BioCAS: Biometeorological Climate impact Assessment System for building-scale impact assessment of heat-stress related mortality. *DIE ERDE—J. Geogr. Soc. Berlin* **2014**, *145*, 62–79. [CrossRef]
6. Fehrenbach, U.; Scherer, D.; Parlow, E. Automated classification of planning objectives for the consideration of climate and air quality in urban and regional planning for the example of the region of Basel/Switzerland. *Atmos. Environ.* **2001**, *35*, 5605–5615. [CrossRef]
7. Eum, J.H.; Scherer, D.; Fehrenbach, U.; Köppel, J.; Woo, J.H. Integrating urban climate into urban master plans using spatially distributed information—The Seoul example. *Land Use Policy* **2013**, *34*, 223–232. [CrossRef]
8. Woo, J.H.; An, S.M.; Hong, K.; Kim, J.J.; Lim, S.B.; Kim, H.S.; Eum, J.H. Integration of CFD-Based Virtual Sensors to A Ubiquitous Sensor Network to Support Micro-Scale Air Quality Management. *J. Environ. Inform.* **2016**, *27*, 85–97. [CrossRef]
9. Yi, C.; Kim, K.R.; An, S.M.; Choi, Y.J.; Holtmann, A.; Jänicke, B.; Fehrenbach, U.; Scherer, D. Estimating spatial patterns of air temperature at building-resolving spatial resolution in Seoul, Korea. *Int. J. Climatol.* **2016**, *36*, 533–549. [CrossRef]
10. Scherer, D.; Antretter, F.; Bender, S.; Cortekar, J.; Emeis, S.; Fehrenbach, U.; Gross, G.; Halbig, G.; Hasse, J.; Maronga, B.; et al. Urban climate under change [UC] 2-A national research programme for developing a building-resolving atmospheric model for entire city regions. *Meteorol. Z.* **2019**, *28*, 95–104. [CrossRef]
11. Venter, Z.S.; Brousse, O.; Esau, I.; Meier, F. Hyperlocal mapping of urban air temperature using remote sensing and crowdsourced weather data. *Remote Sens. Environ.* **2020**, *242*, 111791. [CrossRef]
12. Kim, Y.; An, S.M.; Eum, J.H.; Woo, J.H. Analysis of thermal environment over a small-scale landscape in a densely built-up Asian megacity. *Sustainability* **2016**, *8*, 358. [CrossRef]
13. An, S.M.; Kim, B.S.; Lee, H.Y.; Kim, C.H.; Yi, C.Y.; Eum, J.H.; Woo, J.H. Three-dimensional point cloud based sky view factor analysis in complex urban settings. *Int. J. Climatol.* **2014**, *34*, 2685–2701. [CrossRef]
14. Kong, F.; Yan, W.; Zheng, G.; Yin, H.; Cavan, G.; Zhan, W.; Zhang, N.; Cheng, L. Retrieval of three-dimensional tree canopy and shade using terrestrial laser scanning (TLS) data to analyze the cooling effect of vegetation. *Agric. For. Meteorol.* **2016**, *217*, 22–34. [CrossRef]
15. Trepekli, K.; Balstrøm, T.; Friborg, T.; Fog, B.; Allotey, A.N.; Kofie, R.Y.; Møller-Jensen, L. UAV-borne, LiDAR-based elevation modelling: A method for improving local-scale urban flood risk assessment. *Nat. Hazards* **2022**, *113*, 423–451. [CrossRef]
16. Ramalho de Oliveira, L.F.; Lassiter, H.A.; Wilkinson, B.; Whitley, T.; Ifju, P.; Logan, S.R.; Peter, G.F.; Vogel, J.G.; Martin, T.A. Moving to automated tree inventory: Comparison of uas-derived lidar and photogrammetric data with manual ground estimates. *Remote Sens.* **2021**, *13*, 72. [CrossRef]
17. Feng, Q.; Zhu, D.; Yang, J.; Li, B. Multisource hyperspectral and lidar data fusion for urban land-use mapping based on a modified two-branch convolutional neural network. *ISPRS Int. J. Geoinf.* **2019**, *8*, 28. [CrossRef]
18. Megahed, Y.; Shaker, A.; Yan, W.Y. Fusion of airborne LiDAR point clouds and aerial images for heterogeneous land-use urban mapping. *Remote Sens.* **2021**, *13*, 814. [CrossRef]
19. Nuissl, H.; Siedentop, S. Urbanisation and land use change. In *Sustainable Land Management in a European Context: A Co-Design Approach*; Weith, T., Barkmann, T., Gaasch, N., Rogga, S., Strauß, C., Zscheischler, J., Eds.; Springer Cham: Manhattan, NY, USA, 2021; pp. 75–99. [CrossRef]
20. An, S.M.; An, Y.H.; Kim, I.H. A Study on Digital Twinning Applications for a Land Use with Wind. *Korea Res. Inst. Hum. Settl.* **2021**, *21*, 19–21.

21. An, S.M. A Study on Urban Scale High-Resolution Sky View Factor Mapping and Applications. *Korea Spat. Plan. Rev.* **2022**, *113*, 57–74. [CrossRef]
22. An, S.M.; Lee, H.Y.; Kim, B.; Yi, C.Y.; Eum, J.H.; Woo, J.H. Geospatial spreadsheets with microscale air quality visualization and synchronization for supporting multiple-scenario visual collaboration. *Int. J. Geogr. Inf. Sci.* **2014**, *28*, 2511–2532. [CrossRef]
23. Nogueira, M.S.; Gunther, J.E.; Komolibus, K.; Andersson-Engels, S. User-friendly graphical user interface for simulating tissue optical properties and fluence rates: Improving students learning in tissue optics. In *Optical Interactions with Tissue and Cells XXXI*; SPIE: San Francisco, CA, USA, 2020; Volume 11238, pp. 45–53. [CrossRef]
24. Wang, Y.; Fang, H. Estimation of LAI with the LiDAR technology: A review. *Remote Sens.* **2020**, *12*, 3457. [CrossRef]
25. Yi, C.; An, S.M. A Study on Building Identification from the Three-dimensional Point Cloud by using Monte Carlo Integration Method. *J. Korea Assoc. Geogr. Inf. Stud.* **2020**, *23*, 16–41. [CrossRef]
26. American Society for Photogrammetry & Remote Sensing (ASPRS). *LAS Specification 1.4-R15*; ASPRS: Bethesda, ML, USA, 2019.
27. James, F. Monte Carlo theory and practices. *Rep. Prog. Phys.* **1980**, *43*, 1147–1189. [CrossRef]
28. U.S. Environmental Protection Agency (EPA). *Guiding Principles for Monte Carlo Analysis*; EPA: Washington, DC, USA, 1997.
29. Middel, A.; Lukasczyk, J.; Maciejewski, R.; Demuzere, M.; Roth, M. Sky View Factor footprints for urban climate modeling. *Urban Clim.* **2018**, *25*, 120–134. [CrossRef]
30. Kastendeuch, P.P. A method to estimate sky view factors from digital elevation models. *Int. J. Climatol.* **2013**, *33*, 1574–1578. [CrossRef]
31. Jeon, Y.; Kim, S. Housing abandonment in shrinking cities of East Asia: Case study in Incheon, South Korea. *Urban Stud.* **2020**, *57*, 1749–1767. [CrossRef]
32. Park, M.S.; Lee, H. Smart city crime prevention services: The Incheon free economic zone case. *Sustainability* **2020**, *12*, 5658. [CrossRef]
33. OECD. The Governance of Land Use in Korea: Urban Regeneration. Available online: https://doi.org/10.1787/fae634b4-en (accessed on 8 June 2023).
34. NGII. The National Atlas of KoreaII 2020. Available online: http://nationalatlas.ngii.go.kr/pages/page_2409.php (accessed on 8 June 2023).
35. Lindberg, F.; Olofson, K.F.G.; Sun, T.; Grimmond, C.S.B.; Feigenwinter, C. Urban storage heat flux variability explored using satellite, meteorological and geodata. *Theor. Appl. Climatol.* **2020**, *141*, 271–284. [CrossRef]
36. Verburg, P.H.; Alexander, P.; Evans, T.; Magliocca, N.R.; Malek, Z.; Rounsevell, M.D.; van Vliet, J. Beyond land cover change: Towards a new generation of land use models. *Curr. Opin. Environ. Sustain.* **2019**, *38*, 77–85. [CrossRef]
37. Martins, J.A.C.; Nogueira, K.; Osco, L.P.; Gomes, F.D.G.; Furuya, D.E.G.; Gonçalves, W.N.; Sant'Ana, D.A.; Ramos, A.P.M.; Liesenberg, V.; dos Santos, J.A.; et al. Semantic segmentation of tree-canopy in urban environment with pixel-wise deep learning. *Remote Sens.* **2021**, *13*, 3054. [CrossRef]
38. National Infrastructure Commission. Data for the Public Good. Available online: https://nic.org.uk/app/uploads/Data-for-the-Public-Good-NIC-Report.pdf (accessed on 8 June 2023).
39. Liu, Z.; Cheng, W.; Jim, C.Y.; Morakinyo, T.E.; Shi, Y.; Ng, E. Heat mitigation benefits of urban green and blue infrastructures: A systematic review of modeling techniques, validation and scenario simulation in ENVI-met V4. *Build. Environ.* **2021**, *200*, 107939. [CrossRef]
40. Langer, I.; Pasternack, A.; Ulbrich, U.; Rust, H.W. Messungen der 2m Temperatur und Feuchte zur Evaluierung von PALM-4U (No. DACH2022-70). In Proceedings of the Copernicus Meetings, Leipzig, Deutschland, 21–25 March 2022. [CrossRef]
41. Kedar, J. SmartCity: Digital Twin? Ordnance Survey Development. Available online: https://ggim.un.org/unwgic/presentations/3.5-JOHN-KEDAR.pdf (accessed on 8 June 2023).
42. Hu, J.; Zhang, H.; Irfan, M. How does digital infrastructure construction affect low-carbon development? A multidimensional interpretation of evidence from China. *J. Clean. Prod.* **2023**, *396*, 136467. [CrossRef]
43. Federal Geographic Data Committee (FGDC). *National Spatial Data Infrastructure Strategic Plan 2021–2024*; FGDC: Reston, VA, USA, 2020.
44. O'Neil-Dunne, J.; MacFaden, S.; Royar, A. A versatile, production-oriented approach to high-resolution tree-canopy mapping in urban and suburban landscapes using GEOBIA and data fusion. *Remote Sens.* **2014**, *6*, 12837–12865. [CrossRef]
45. Wong, K.K.Y. Towards a National 3D Mapping Product for Great Britain. Ph.D. Thesis, University College London, London, UK, 2018.
46. Ren, Y.; Lü, Y.; Comber, A.; Fu, B.; Harris, P.; Wu, L. Spatially explicit simulation of land use/land cover changes: Current coverage and future prospects. *Earth Sci. Rev.* **2019**, *190*, 398–415. [CrossRef]
47. Zhang, X.; Liu, L.; Chen, X.; Gao, Y.; Xie, S.; Mi, J. GLC_FCS30: Global land-cover product with fine classification system at 30 m using time-series Landsat imagery. *Earth Syst. Sci. Data* **2021**, *13*, 2753–2776. [CrossRef]
48. Li, D.; Huang, Y.; Xiao, Y.; He, M.; Wen, J.; Li, Y.; Ma, M. Evaluation of the High-Resolution MuSyQ LAI Product over Heterogeneous Land Surfaces. *Remote Sens.* **2023**, *15*, 1238. [CrossRef]
49. Ekim, B.; Sertel, E. Deep neural network ensembles for remote sensing land cover and land use classification. *Int. J. Digit. Earth* **2021**, *14*, 1868–1881. [CrossRef]
50. Kalita, I.; Roy, M. Deep neural network-based heterogeneous domain adaptation using ensemble decision making in land cover classification. *IEEE Trans. Artif. Intell.* **2020**, *1*, 167–180. [CrossRef]

51. Levoy, M. Spreadsheets for Images. In Proceedings of the 21st Annual Conference on Computer Graphics and Interactive Techniques, Los Angeles, CA, USA, 24 July 1994; pp. 139–146.
52. Chi, E.H.; Riedl, J.; Barry, P.; Riedl, J.; Konstan, J. Principles for information visualization spreadsheets. *IEEE Comput. Graph. Appl.* **1998**, *18*, 30–38. [CrossRef]
53. Griffin, A.L.; White, T.; Fish, C.; Tomio, B.; Huang, H.; Sluter, C.R.; Bravo, J.V.M.; Fabrikant, S.I.; Bleisch, S.; Yamada, M.; et al. Designing across map use contexts: A research agenda. *Int. J. Cartogr.* **2017**, *3*, 90–114. [CrossRef]